New seismic constraints on the upper mantle structure of the Hainan plume

Jianshe Lei [a,*], Dapeng Zhao [b], Bernhard Steinberger [c], Bateer Wu [d], Fanluan Shen [e], Zhixiong Li [e]

[a] Institute of Crustal Dynamics, China Earthquake Administration, Beijing 100085, China
[b] Department of Geophysics, Tohoku University, Sendai 980-8578, Japan
[c] Center for Geodynamics, Norges Geologiske Undersøkelse, Leiv Eirikssons vei 39, N-7491 Trondheim, Norway
[d] Department of Geophysics, College of Preventing Disaster Technique, Yanjiao 065201, China
[e] Seismological Bureau of Hainan Province, Haikou 570203, China

ARTICLE INFO

ABSTRACT

We present a high-resolution tomographic image in the upper mantle for the Hainan plume determined by using both local and teleseismic data. The arrival-time data from teleseismic events are measured precisely from seismograms recorded by nine permanent seismic stations in Hainan island and Leizhou peninsula. Our results show that striking low-velocity (low-V) anomalies of up to −5% in the crust and −2% in the mantle are visible under the Hainan hotspot from the surface down to 250 km depth. The Hainan plume is imaged as a continuous, NW–SE tilting, low-V column with a diameter of about 80 km. Given the denser data coverage and finer parameterization, our result represents a significant improvement with respect to earlier, regional and global tomographic studies. Such an inclination of the Hainan plume can be explained by numerical simulations. The tilted plume conduit in the upper mantle could be associated with the subduction of oceanic plates, especially the Philippine Sea plate, and the extrusion of the Eurasian plate. Most likely, the tilted plume conduit has buoyantly risen from the lower mantle.

© 2008 Elsevier B.V. All rights reserved.

1. Introduction

There are a variety of tectonic features in East Asia that are controlled by the collision of the Indian and Eurasian plates and the subduction of the Philippine Sea and Pacific plates (e.g., Molnar and Tapponnier, 1975; Tapponnier et al., 1986; Yin and Harrison, 2000; Zhao, 2004; Lei and Zhao, 2005, 2007a), such as the formation of the Tibetan plateau, Tien Shan orogenic belt, active large fault zones, large earthquakes, and active intraplate volcanoes (Fig. 1). In mainland China there are a number of active and Quaternary volcanoes, such as the Changbai, Wudalianchi, Tengchong, Datong, Kunlun, Tianshan, and Hainan volcanoes (Liu, 1999, 2000) (Fig. 1). Among these volcanoes, the first two are considered to be active back-arc volcanoes, which may be caused by the deep dehydration of the subducted Pacific slab in the mantle transition zone (e.g., Zhao, 2004; Lei and Zhao, 2005; Huang and Zhao, 2006). The Hainan volcano is situated at the Hainan island which is in the southernmost portion of the South China block and is separated from mainland China by the Qiongzhou strait (Figs. 1 and 2). The Hainan volcano has erupted many times since the Eocene. The Pliocene and Quaternary volcanism at the Hainan island can be grouped into two major eruptive stages, Late Tertiary and Quaternary, which are distributed in six eruption areas, Chinniuling, Penglei-Geding, Lungtang, Yangpukang, Towenling, and Maanling (Ho et al., 2000) (Fig. 2). The early volcanism was dominated by flood type fissure eruption of quartz tholeiites and olivine tholeiites, while the later phase was dominated by central type eruption of alkali olivine basalts and olivine tholeiites (Ho et al., 2000). The basaltic lava flows are widely distributed and occupy an area (including Leizhou peninsula) of over 7000 km^2. Such a strong activity of Cenozoic magmatism may be related to the deep structure and tectonics of the region. The Hainan plume was termed by Lebedev et al. (2000), and some recent studies have suggested that Hainan may be a volcano of hotspot-type (e.g., Lebedev and Nolet, 2003; Liang et al., 2004; Montelli et al., 2004a,b).

Forty-five years ago Wilson (1963) suggested the existence of hotspots on the Earth, which are usually characterized by topographic swell, higher temperature, and recent volcanism with isotopic signatures distinct from those that characterize mid-ocean ridge or andesitic basalts (Davies, 1988; Sleep, 1990; Courtillot et al., 2003). Subsequently, Morgan (1971) proposed the existence of mantle plumes to explain hotspot volcanoes such as Hawaii and Iceland. Many researchers have used geochemical and geophysical approaches to study the Hainan volcanism (e.g., Zhu and Wang, 1989; Tu et al., 1991; Zhang et al., 1996; Ho et al., 2000; Lebedev et al., 2000; Friederich, 2003; Lebedev and Nolet, 2003; Liang et al., 2004; Montelli et al., 2004a,b), though few geochemists consider it to be of hotspot type. Late Cenozoic volcanic activity was very inten-

* Corresponding author. Tel.: +86 10 6284 6760; fax: +86 10 6292 7306.
E-mail addresses: leijs@hotmail.com, leijs@eq-icd.cn, leijs@eyou.com (J. Lei).
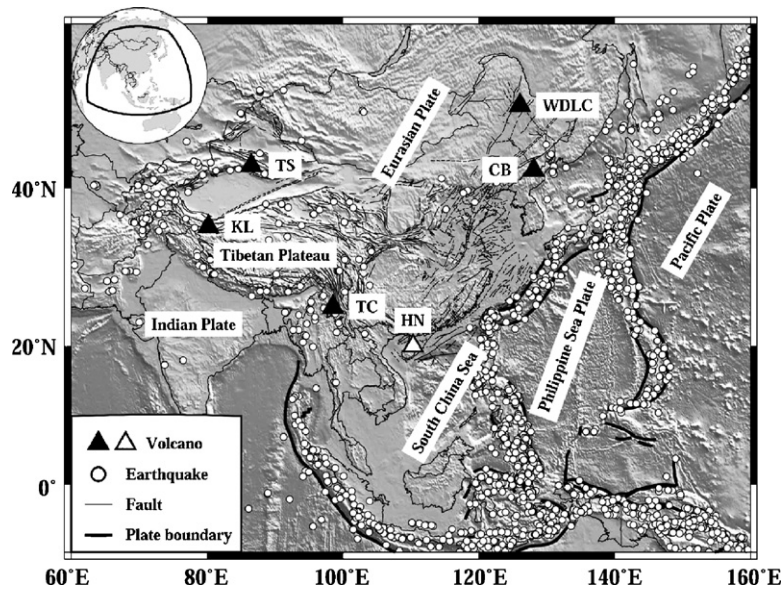
Fig. 1. Location of the Hainan hotspot (white triangle, HN) and topography map of East Asia. Black triangles denote the Wudalianchi (WDLC), Changbai (CB), Tengchong (TC), Tianshan (TS), and Kunlun (KL) volcanoes in mainland China. Dots denote the earthquakes relocated by Engdahl et al. (1998). Thin traces represent active faults in China. Thick lines denote the plate boundaries.

sive in the Hainan region, where magmas were erupted through a relatively young (late Paleozoic) and thin (<33 km) continental crust (Zhou and Armstrong, 1982). Some shallower geophysical features of the Hainan island were summarized by Liu (2000) as follows: (1) a thin continental crust 31–33 km thick; (2) a high heat flow of up to 87 mW/m^2; (3) a very high vertical geothermal gradient of 5.5–8.0 °C/100 m; (4) a low-velocity (low-V) anomaly 1–3 km thick at 6-11 km depth in the crust; and (5) a lower resistivity layer about 5 km thick at 6.3–11.6 km depth below the surface. Pn arrival-time data show a low-V anomaly around the Hainan island in the upper-most mantle (Liang et al., 2004). Regional travel-time tomography revealed low-V anomalies down to 200 km depth (Lei and Zhou, 2002) and from the surface down to 1300 km depth (Huang and Zhao, 2006) beneath the Hainan region. Surface-wave tomography of East Asia shows a low-V anomaly beneath the Hainan island from the crust to a depth of about 660 km (Lebedev and Nolet, 2003). Friederich (2003) also displays a similar low-V anomaly but its depth range does not exceed 450 km perhaps because Hainan is near the southern edge of his study region. Global tomographic models show the existence of a low-V anomaly beneath the Hainan hotspot extending down to about 1900 km depth (e.g., Ritsema et al., 1999; Montelli et al., 2006) or to the lowermost mantle (e.g., Zhao, 2001, 2004; Antolik et al., 2003; Lei and Zhao, 2006a). How-ever, all these models have a spatial resolution of 200–500 km or larger and so they cannot display a detailed morphology of the Hainan plume in the crust and upper mantle.

The Hainan seismic network has been in operation since 1999 and it consists of nine digital seismic stations. A few studies have been conducted to investigate the deep structure under Hainan by applying the receiver function technique to the data recorded by the broadband seismic station QIZ of the Hainan network (Yang and Zhou, 2001; Qiu et al., 2006). These results showed the exis-tence of a thin mantle transition zone under QIZ. However, no tomographic study has been made using the new data set from the Hainan seismic network. The availability of high-quality and abundant local and teleseismic data recorded by this seismic net-work allows us to determine a detailed 3D velocity structure of the crust and upper mantle to understand the origin of the Hainan volcanism.

In this study we have applied a new tomographic method to both local and teleseismic data recorded by the Hainan seismic network to determine the upper mantle structure under the Hainan island and adjacent regions. Our results provide new constraints on the nature of the Hainan plume.
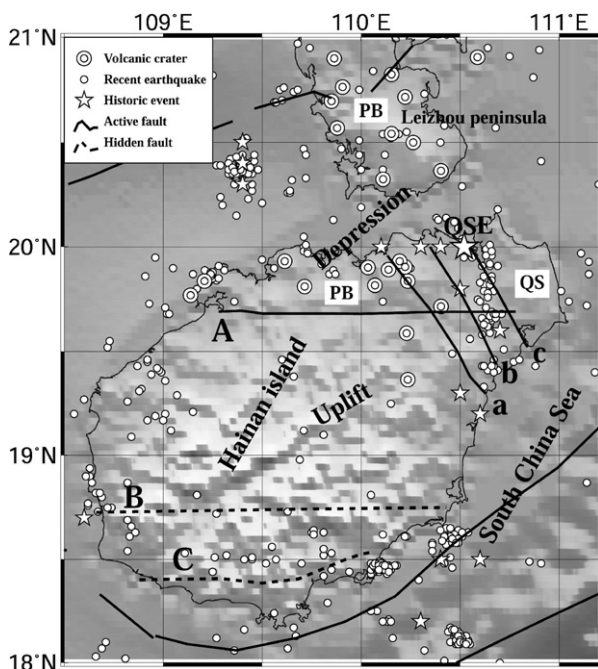
Fig. 2. Regional tectonic features in Hainan island and adjacent areas and distribu-tion of 464 local earthquakes (white circles) used in the study. Double circles denote volcanic craters. Stars represent the historic earthquakes since the year 1400. The big star (QSE) denotes the 1605 (*M* 7.5) Qiongshan earthquake. White dots denote recent earthquakes recorded by the Hainan seismic network during 2002–2006. The traces denote major faults in and around Hainan island. A, Wangwu-Wenjiao fault; B, Jianfeng-Diaoluo fault; C, Jiusuo-Lingshui fault. a, Changliu-Xiangou fault; b, Haikou-Yunlong fault; c, Puqian-Qinglan fault. PB, Pleistocene basalt; QS, Quater-nary sediment. The traces of the faults and the locations of the volcanic craters were scanned from Ma (1989).

2. Tectonic setting

Hainan island is located near the southeastern margin of the Eurasian plate, and has been affected by the motions and interaction of the Indian and Philippine Sea plates and by the extension of the South China Sea basin (Fig. 1). Hence this region has been affected by complex tectonics, frequent volcanic eruptions and large earthquake shakings (Ma, 1989; Li, 1991) (Fig. 2). These phenomena were mainly caused by the extension of the South China Sea basin, which is a back-arc basin resulting from extension with an approximate EW trend. The extension caused a series of depressions, uplifts, and right-lateral strike-slip faults from South China Sea to mainland China (Liu and Zhang, 1989; Li, 1991) (Fig. 2).

Major active faults in the region can be sorted into two types, E-W oriented faults, and NW–SE oriented faults (Fig. 2). The E-W oriented faults are deeper and larger, such as the Wangwu-Wenjiao, Jianfeng-Diaoluo and Jiusuo-Lingshui faults, which are closely related to the distribution of depressions, uplifts and volcanic rocks in the region. The Wangwu-Wenjiao fault is at the boundary between some depressions in the Lei-Qiong region and some uplifts in the central and southern areas of Hainan island. Active volcanoes and earthquakes are distributed north of the Wangwu-Wenjiao fault (Fig. 2), while the area from the Wangwu-Wenjiao fault to the Jianfeng-Diaoluo fault is relatively stable (Liu and Zhang, 1989; Li, 1991). Toward the south, seismicity becomes active south of the Jianfeng-Diaoluo fault, where many moderate-to-strong earthquakes as well as swarms of small earthquakes occurred (Hu et al., 1997; Chen et al., 2002).

North of the Wangwu-Wenjiao fault, the NW-SE oriented faults are neogenic and active, and they are closely associated with the most recent volcanic activity and the distribution of the Neozoic stratification. These faults are distributed uniformly with a spatial separation of 30–40 km, such as the Changliu-Xiangou fault, the Haikou-Yunlong fault, and the Puqian-Qinglan fault (Fig. 2). These NW–SE faults have generated strong earthquakes, such as the 1605 Qiongshan earthquake (*M* 7.5). Therefore, it is of great importance to study the crust and upper mantle structure under the Hainan region for understanding the seismotectonics in the region in addition to the Hainan volcanism.
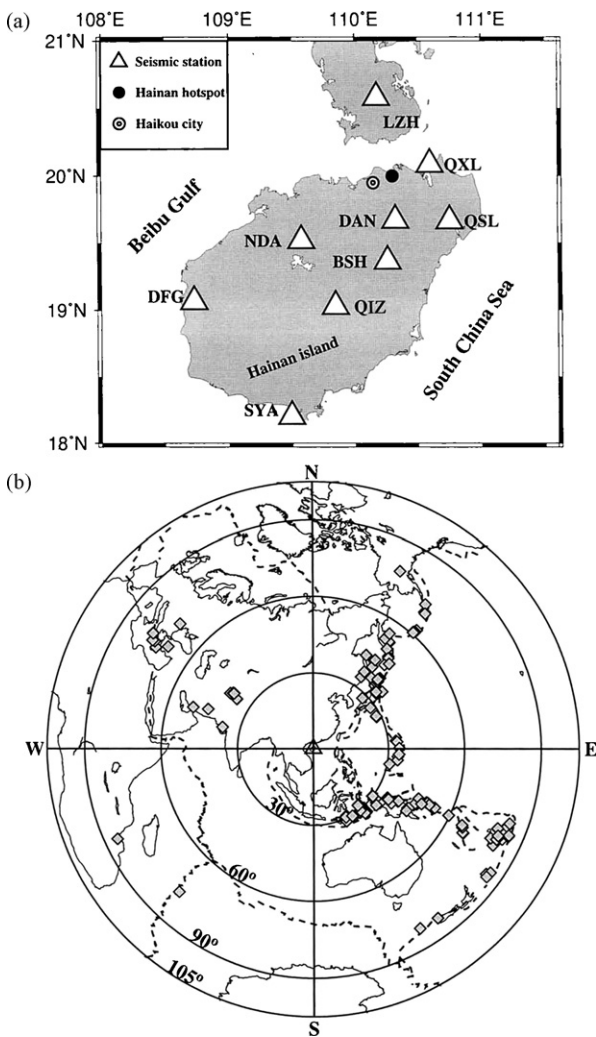

Fig. 3. (a) Distribution of nine seismic stations (triangles) used in this study. The station code is shown beside each station. The black dot denotes the Hainan hotspot, while the double circle denotes the location of Haikou city. (b) Azimuthal distribution of teleseismic events (diamonds) used in the study. The hypocenter parameters were determined by Dr. E. Engdahl with a procedure described by Engdahl et al. (1998). The numbers represent the epicentral distances in degrees (1° = 111.2 km). The triangle denotes the center of the study area.
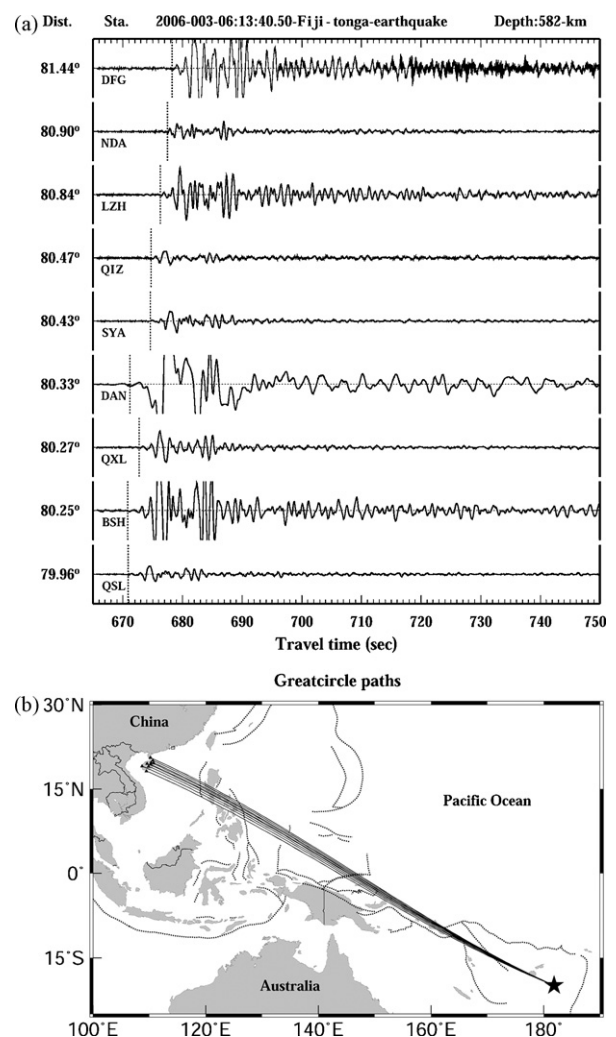
Fig. 4. (a) An example showing original vertical-component seismograms recorded by the Hainan seismic network for an earthquake (*M* 7.2) occurred in the Fiji-Tonga region on January 3, 2006. The vertical dashed lines show the P first arrivals we picked. The letters and numbers on the left denote the corresponding seismic stations and epicentral distances in degrees, respectively. (b) Great circle paths for the traces in (a). The star denotes the epicenter, and triangles show the seismic stations in Hainan island. Dotted lines represent the tectonic boundaries.
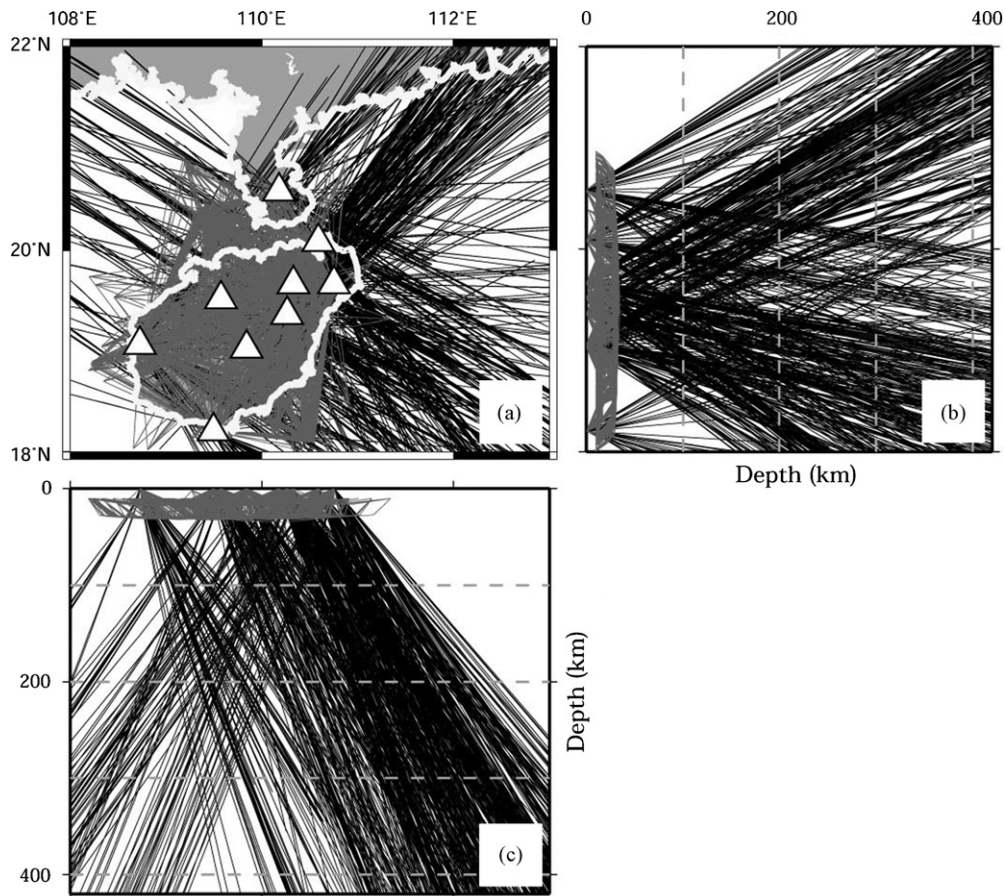
Fig. 5. Distribution of P-wave ray paths used in this study in (a) map view and in (b) the north–south and (c) east–west vertical cross-sections. Gray lines denote the ray paths of the local data, while black lines represent the ray paths of the teleseismic data. White triangles denote the seismic stations used in this study. White curves represent the coastlines.

3. Data and method

Fig. 3a shows the distribution of nine digital seismic stations used in this study. Except for three-component broadband seismometers at station QIZ, the other eight stations are all equipped with short-period sensors. These stations have been operating formally since 1999, and a large amount of high-quality waveform data have been accumulated, thanks to the very low noise level in the less industrialized Hainan island (Fig. 4). These stations cover the entire Hainan island and southern Leizhou peninsula, but they are unevenly distributed in the region. In NE Hainan there are more stations, while only one station (SYA) exists in southern Hainan and one station (DFG) in western Hainan.

In this study both local and teleseismic first P-wave arrival times are collected. Over 3500 high-quality local arrival times are selected from 464 earthquakes. These local events are mainly distributed on the margins of Hainan island (Fig. 2). The local rays used are illustrated in Fig. 5. We collected carefully over 850 high-quality teleseismic P-wave arrivals from high-quality original seismograms (Fig. 4) of 138 teleseismic events (Fig. 3b) after examining over 1500 earthquakes that occurred from 2002 to 2006. All these local and teleseismic events have at least five recordings, respectively, and the picking accuracy of the arrival-time data is estimated to be 0.10–0.15 s. We relocated the local earthquakes using the double-difference location method (Waldhauser and Ellsworth, 2000) and used the teleseismic hypocenter parameters determined by Dr. Engdahl (see Engdahl et al. (1998) for the location procedure). The magnitude of these teleseismic events is greater than 4.8. The

events selected have an epicentral distance between 28° and 90° from the center of the network, while their azimuthal distribution is not uniform (Fig. 3b). Most of them are located in the subduction zones of the northern and western Pacific, and a few are in central Asia and the Indian Ocean. The teleseismic rays used in this study are also shown in Fig. 5. Fig. 6a and c illustrates the histograms of absolute travel-time residuals of the local data and relative travel-time residuals of the teleseismic data calculated for the initial 1D model (Fig. 7).

Taking into account the Earth's ellipticity (Dziewonski and Gilbert, 1976) and the station elevations, we compute the theoretical travel times by using an updated version of the 3D ray tracer by Zhao (2001) for the 1D initial model (Fig. 7) that is summarized from the previous studies (Qiu et al., 2006; Ding et al., 2004; Jia et al., 2006) for the crust and by adopting the iasp91 Earth model (Kennett and Engdahl, 1991) for the mantle. This 3D ray tracer can calculate the travel times and ray paths for both local and teleseismic events efficiently and accurately, and can deal with a velocity model containing velocity discontinuities of complex geometry and 3D velocity variation everywhere in the model. For details, see Zhao et al. (1992) and Zhao and Lei (2004). To calculate the travel times accurately, in the present study we have taken into account depth variations of the Moho discontinuity (Fig. 8) which were determined by using gravity data (Li et al., 2006). In order to minimize the effect of the uncertainties in hypocenter locations and origin times, as well as the velocity heterogeneities outside of the study area, we used relative travel-time residuals of the teleseismic events in the tomographic inversion. For details of the calculation of the relative
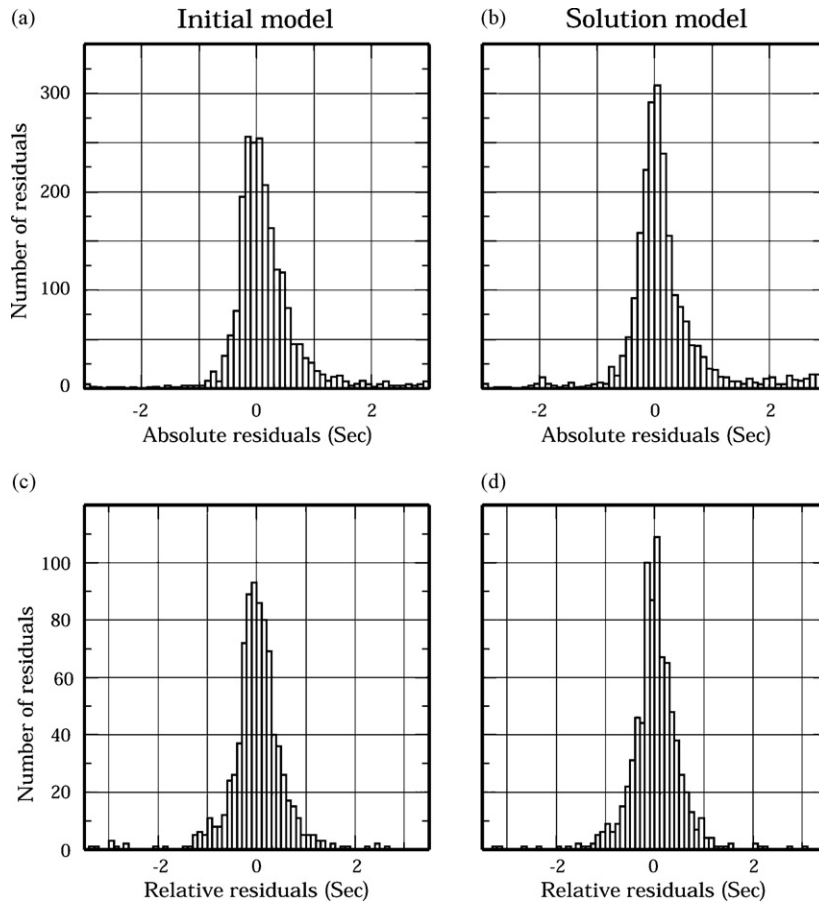
Fig. 6. Histograms of the travel-time residuals. (a and b) The absolute residuals from the local data. (c and d) The relative residuals from the teleseismic data. (a and c) are obtained for the initial model (Fig. 7), while (b and d) are inferred from the solution model.

residuals, see Zhao et al. (1994) and Lei and Zhao (2005). When calculating the travel times of the teleseismic events, we determined the teleseismic ray paths between the hypocenter and receiver and found the intersection between the ray and the boundary plane of the modeling space. Then we determined the ray path between the intersection and the station.

Fig. 9 shows the distribution of the average relative travel-time residuals at all the stations, which shows a clear pattern of delayed and early arrivals. Delayed arrivals are visible at stations LZH and QSL in Leizhou peninsula and northern Hainan, where numerous Neogene/Quaternary volcanoes exist (Fig. 2), while early arrivals are observed at stations in other areas, which correspond to the tectonically relatively stable regions. Although early arrivals are observed at stations NDA and QIZ, their amplitudes are much smaller. The maximum amplitude of delayed arrivals (0.4 s) is larger than that of early arrivals (0.3 s), which suggests the existence of stronger low-V anomalies in the upper mantle under northern Hainan and southern Leizhou peninsula.

We applied the tomographic method of Zhao et al. (1994) to the absolute residuals of local earthquakes and relative residuals of teleseismic events for determining the 3D velocity structure under Hainan. A 3D grid was set up in the model and velocity perturbations at the grid nodes were taken as unknown parameters. In the model the lateral grid spacing is $0.5° \times 0.5°$ and the vertical grid spacing is 4–10 km in the crust and 50 km in the upper mantle. The velocity perturbation at any point in the model was obtained by interpolating the velocity perturbations at the eight grid nodes surrounding that point. A conjugate gradient algorithm (Paige and Saunders, 1982) with damping and smoothing regulations (Zhao,

2001; Lei and Zhao, 2006a) was used to invert the large and sparse system of observation equations.

To obtain a suitable damping parameter used in the present study, numerous inversions with different damping parameters have been performed to form a trade-off or L-shaped curve (Fig. 10) that can measure the misfit of each solution model to the data (Eberhart-Phillips, 1986; Hansen, 1992; Ekström et al., 1997; Boschi, 2006; Lei and Zhao, 2007a). An optimal damping parameter is usually thought of as that corresponding to the maximum curvature of the L-shaped curve (e.g., Hansen, 1992; Boschi, 2006; Boschi et al., 2006). Following this criterion, we took a damping value of 12.0 (Fig. 10) to invert for our final solution model (Figs. 11 and 12a–c).

4. Results and resolution analyses

Teleseismic rays are nearly vertical and do not have a sufficient path coverage in the crust (Fig. 5). Therefore, it is difficult to resolve the crust structure if teleseismic rays are used alone. Poor constraints of the crust structure would certainly affect the mantle image (Lei and Zhao, 2007a). To obtain a reliable mantle structure, some researchers corrected the teleseismic travel-time data by using the previous crust models (e.g., Allen et al., 2002; Hung et al., 2004; Lei and Zhao, 2005, 2007a,b; Zhao et al., 2006). Local rays are almost horizontal, so seismic rays crisscross well in the crust if local and teleseismic data are used jointly; as a result, both the crust and mantle structures are constrained better. For more details of the effect of the local and teleseismic data on the image, see Section 5.1. In the present section we mainly discuss the tomographic model (Figs. 11 and 12a–c) obtained from both local and teleseismic
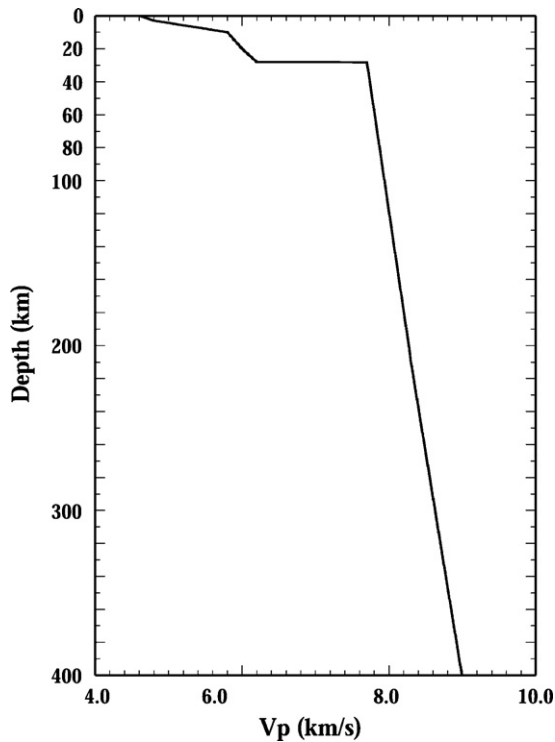
Fig. 7. (a) The starting 1D model used for the tomographic inversion in this study. The model in the crust is summarized from the previous results (Ding et al., 2004; Jia et al., 2006; Li et al., 2006), while that in the mantle is the iasp91 velocity model (Kennett and Engdahl, 1991).

data. It can be seen clearly from Fig. 6 that for our final 3D velocity model both the absolute residuals of the local data and the relative residuals of the teleseismic data are reduced significantly compared with those for the initial 1D model. In particular, the number of the teleseismic relative residuals within 0.1 s is increased from 187 for the initial model to 214 for the final 3D model, and the number of the absolute residuals of local earthquakes within 0.1 s is increased from 504 for the initial model to 625 for the 3D model.
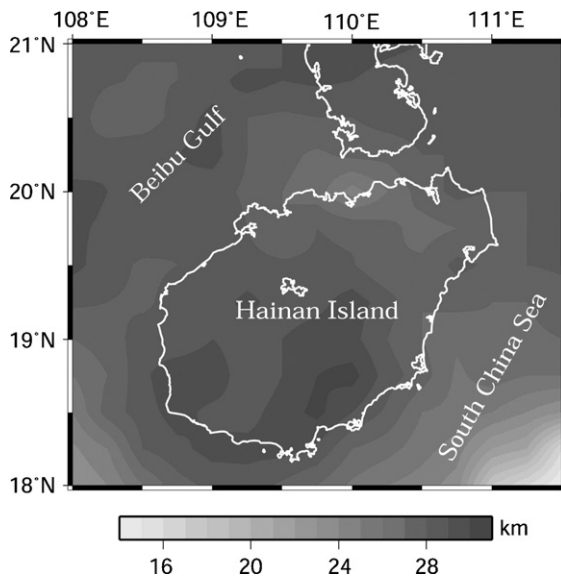

Fig. 8. Illustration of the Moho discontinuity beneath the Hainan and adjacent regions (Li et al., 2006). This model was inferred from gravity data. Depth scale (in km) is shown at the bottom.
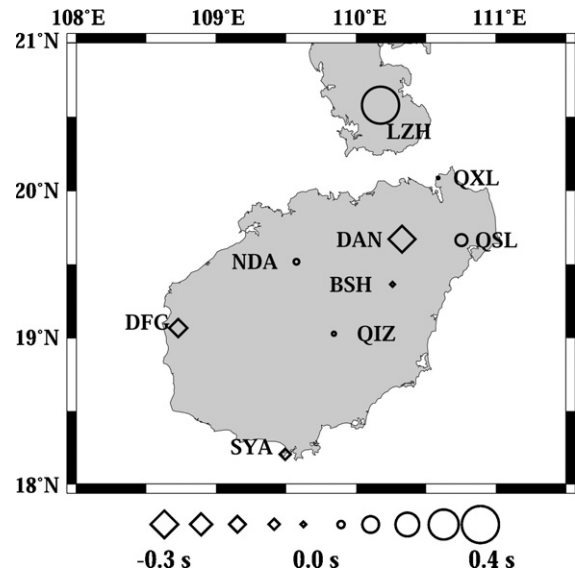

Fig. 9. Distribution of the relative travel-time residuals at each of the nine seismic stations. Diamonds and circles denote negative and positive residuals, respectively. The scale for the residuals (in s) is shown at the bottom.

Fig. 11 shows our final tomographic images in map view. At 1 km depth a prominent low-V anomaly is visible from NE Hainan to Leizhou peninsula through Qiongzhou strait, while south of the Wangwu-Wenjiao fault obvious high velocity (high-V) anomalies are observed (Fig. 11a). Such a pattern of velocity anomalies of up to 5% extends down to 35 km depth (Fig. 11b–f), suggesting that the Wangwu-Wenjiao fault may extend through the Moho discontinuity to the uppermost mantle. High-V anomalies south of the Wangwu-Wenjiao fault are revealed in the crust under the relatively stable uplift, while low-V anomalies are observed in and around Leizhou peninsula (Fig. 11b–f) that is an active Quaternary volcanic area (Fig. 2). However, there are still some changes in the pattern of anomalies from the shallow crust down to the uppermost mantle. For example, under NE Hainan island, low-V anomalies are visible at 1 km depth (Fig. 11a) and they become weaker at 5 km depth (Fig. 11b), while in deeper layers down to 15 km depth they change to high-V anomalies (Fig. 11c and d). At and below 35 km depth high-V anomalies are revealed in western Hainan, while low-V anomalies are visible in eastern Hainan (Fig. 11e and f). The pattern of velocity anomalies is complex in the crust, per-
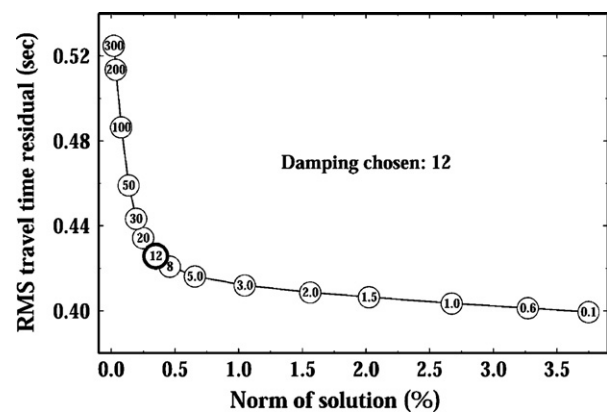
Fig. 10. Trade-off or L-shaped curve for the RMS travel-time residuals versus the variance of the velocity perturbations. Numbers inside the open circles denote the damping parameters adopted for the inversions. The thicker circle denotes the optimal damping parameter (12.0) for the final tomographic model.
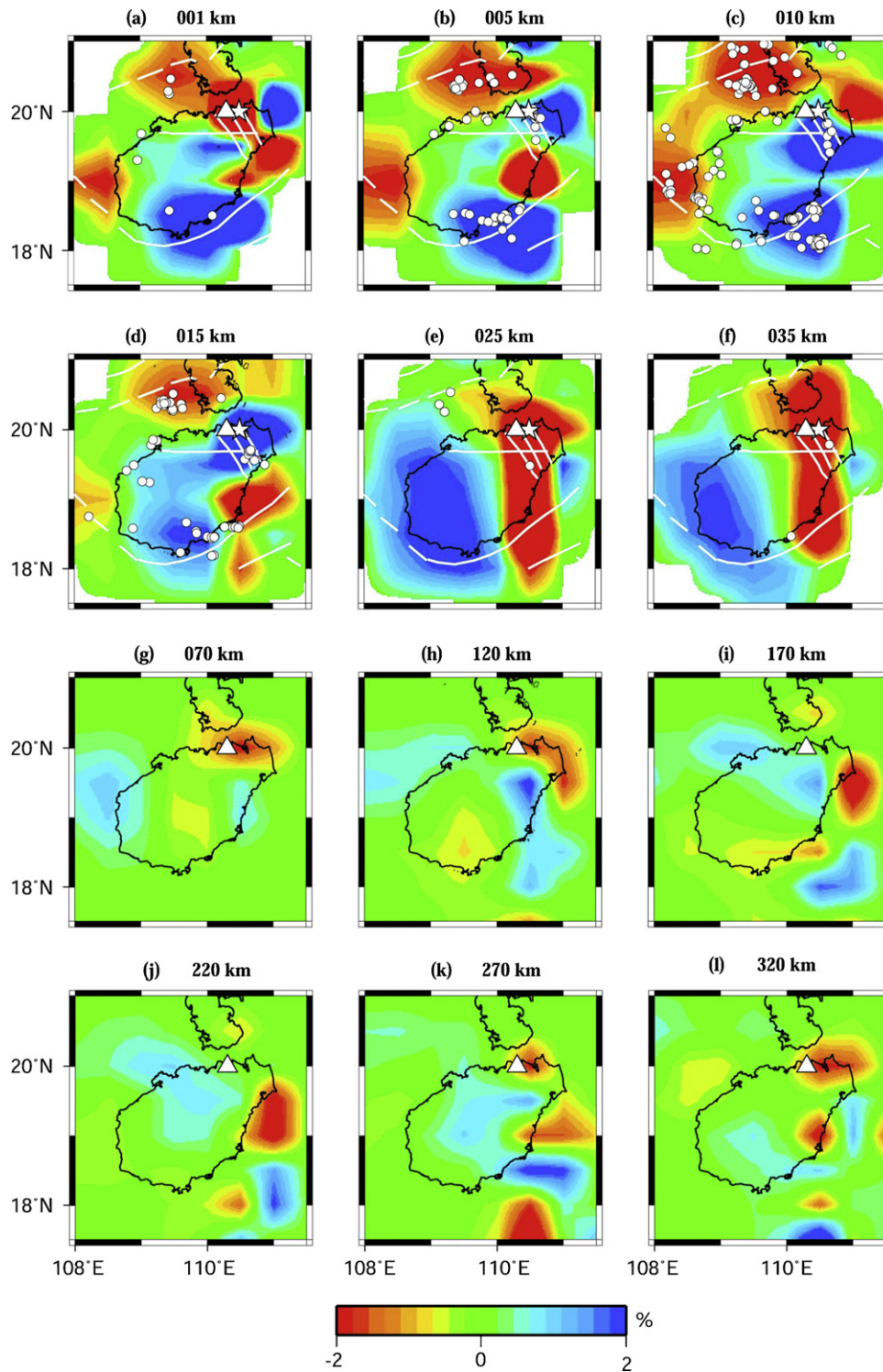
Fig. 11. Map view of P-wave velocity perturbations (in %) inferred from both local and teleseismic data with respect to the initial 1D model as shown in Fig. 7 (see text for details). The layer depth is shown above each map. Red and blue colors denote slow and fast velocity anomalies, respectively. The velocity perturbation scale is shown at the bottom. White and black lines denote active faults and the coastlines, respectively. White circles denote the earthquakes within half distances between two neighboring layers. The triangles indicate the Hainan hotspot. The stars represent the 1605 Qiongshan earthquake.

haps reflecting a strong heterogeneity in the crust. In the mantle the amplitude of velocity anomalies is reduced, and the morphology of low-V anomalies is changed with depth (Fig. 11g–l). Striking low-V anomalies of −2% are clearly visible at depths of 70 and 120 km under NE Hainan and Qiongzhou strait (Fig. 11g and h), and they move gradually toward the southeast with depth (Fig. 11h–l).

Fig. 11a–d shows that most faults pass through low-V anomalies in the shallow crust except for those south of Hainan. The faults may represent fracture zones in the crust or lithosphere. The correlation of the NW-SE oriented faults (e.g., Puqian-Qinglan fault) with low-V anomalies is visible at a much shallower depth range in NE Hainan, perhaps reflecting a much shallower depth extent of these faults.

This is in agreement with the results of deep seismic soundings (Jia et al., 2006). In addition, the distribution of earthquakes is closely related to the orientation of the NW-SE oriented faults in NE Hainan (Fig. 11b and c).

Fig. 12a–c illustrates our final tomographic images along three vertical cross sections. From the N-S and E-W cross sections it is visible that prominent low-V anomalies extend down to only about 150 km depth (Fig. 12a and b), while in the NW-SE cross section the Hainan plume is imaged clearly as a continuous and deflected low-V anomaly from the surface down to 250 km depth (Fig. 12c). These results suggest that the Hainan plume ascends from a depth southeast of Hainan island.

The estimation of the resolution matrix is generally considered to be preferable to the checkerboard/synthetic tests (e.g., Leveque et al., 1993; Barmin et al., 2001; Boschi, 2003), but the former is computationally heavy and it cannot be directly obtained during the inversion if one uses the LSQR algorithm. Therefore, the resolution of the tomographic images is evaluated through synthetic

tests in most of the tomographic studies. In order to evaluate the resolvability of our data set and to confirm the main features of our tomographic image, three kinds of resolution tests (e.g., Zhao et al., 1994; Lei and Zhao, 2005, 2007a,b) were carried out. The first is a checkerboard resolution test for examining the spatial resolution of our tomographic image in the entire study area (Figs. 13 and 14). The second is synthetic tests that are designed to determine whether the assumed plume-like structure can indeed be resolved (Fig. 15). The third is a restoring test for our obtained tomographic model (Fig. 16). The checkerboard resolution test and restoring test are just special forms of a synthetic test. The only difference between them is in the input model. The numbers of seismic stations, events, and ray paths are the same as those in the real data set. Random noises having a normal distribution with zero mean and a standard deviation of 0.1 s were added to the synthetic travel times to simulate the data errors which are usually present in a real data set. By considering our data set as mentioned above, the model has been parameterized with an optimal grid spacing of 0.5° × 0.5° laterally
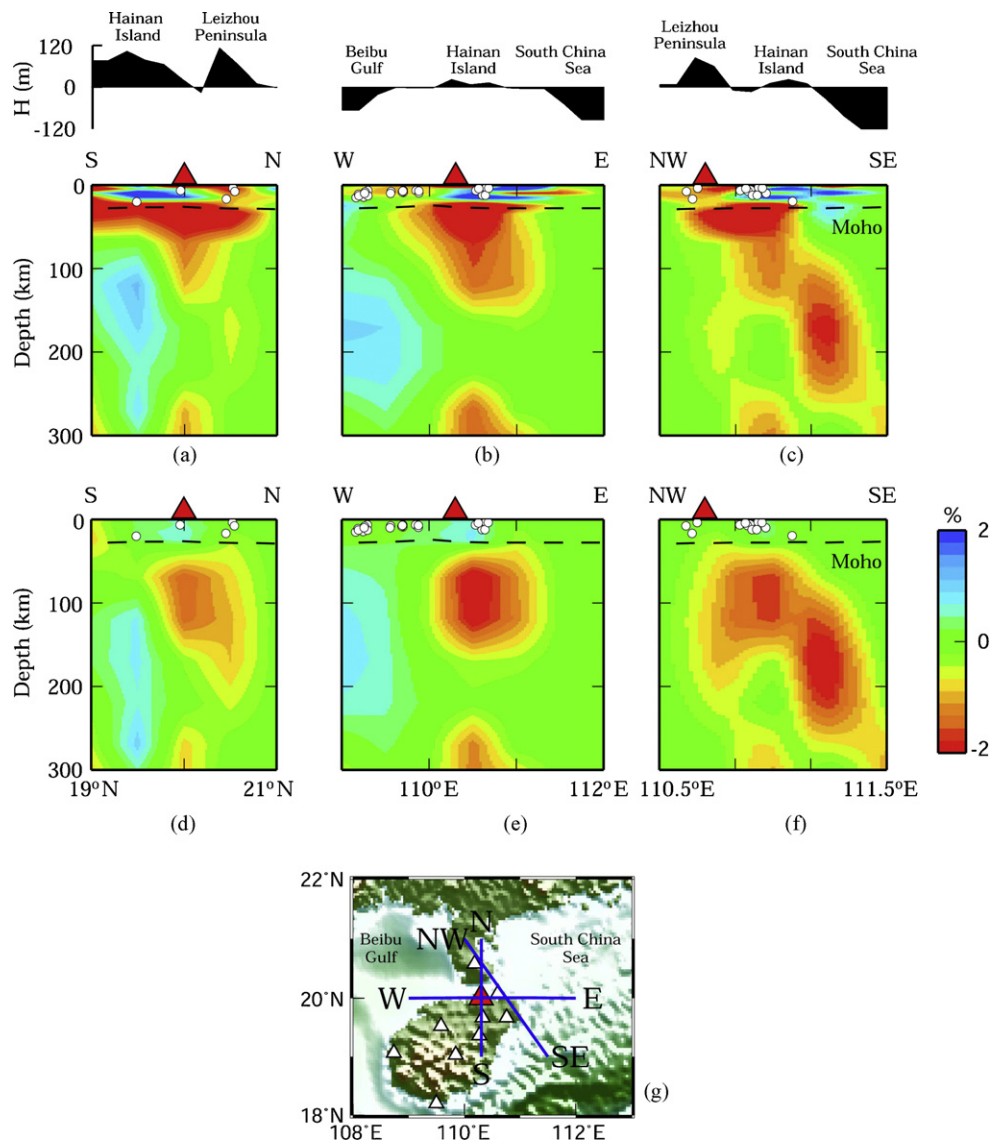
Fig. 12. (a–c) The same as Fig. 11 but for vertical cross-sections as shown in the insert map (g). (d–f) The tomographic image determined only from the teleseismic data. Note that the same parameterization is used in these two models from the crust to the upper mantle. Red and blue colors denote the slow and fast anomalies, respectively. The scale for the velocity perturbation (in %) is shown on the right of (f). Polygons on the top of (a–c) show the surface topography along each cross-section. Dashed lines in (a–f) denote the Moho discontinuity. White dots denote earthquakes that occurred in a range of 25 km off the profiles. The red triangles denote the Hainan hotspot. White triangles in (g) denote seismic stations. No vertical exaggerations (except for surface topography shown) here and in Figs. 14–16.
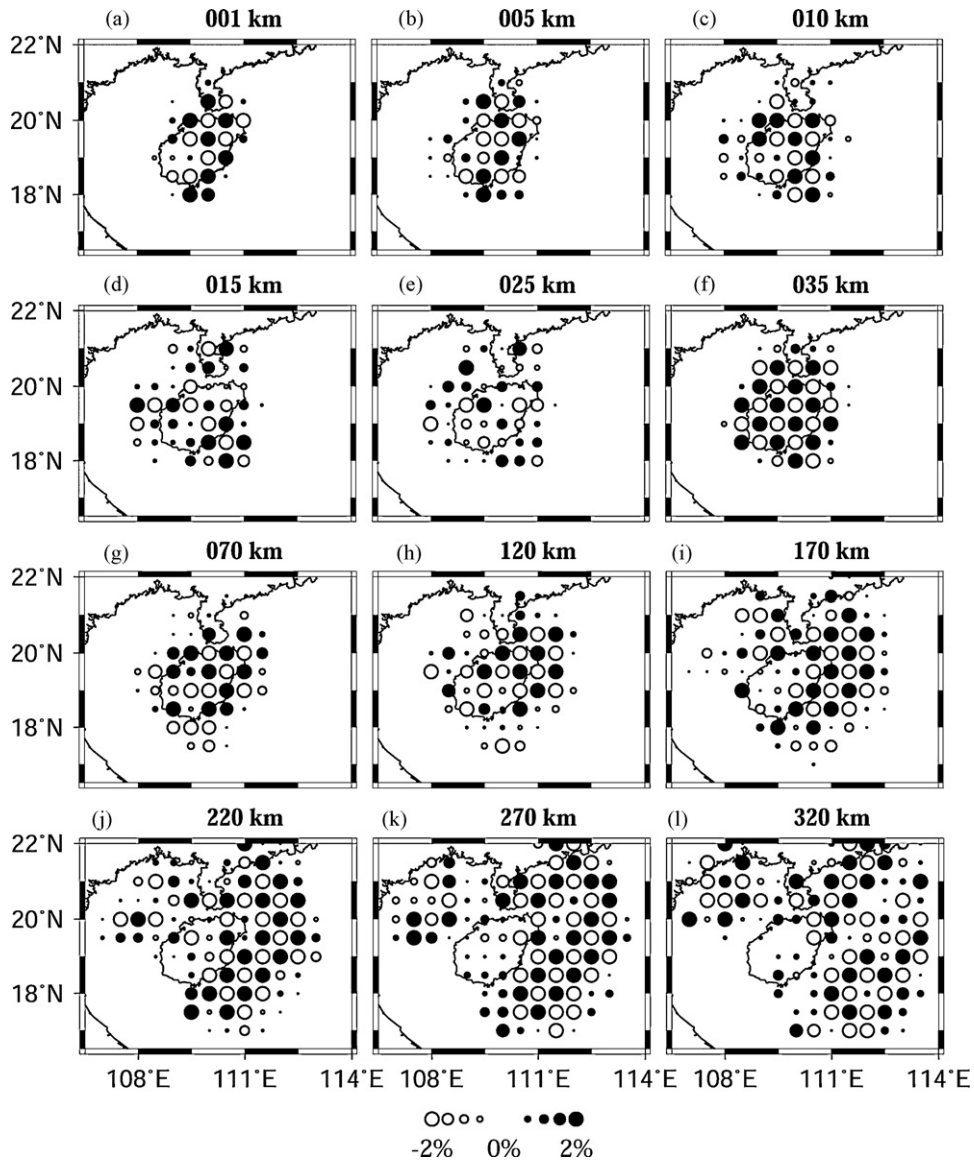
Fig. 13. Results of the checkerboard resolution test for the P-wave structure in map view using both the local and teleseismic data, based on the starting model as shown in Fig. 7. The model is parameterized with a grid spacing of 0.5° × 0.5° in the horizontal directions and 4–50 km in depth. The layer depth is shown above each map. Open and solid circles denote slow and fast velocity anomalies, respectively. The scale for the velocity perturbation (in %) is shown at the bottom.

and 4–10 km in the crust and 50 km in the mantle vertically after making many resolution tests with different grid spacings, because such a parameterization can reflect the teconic features well, and also provide the reliable information on the deep structure in the region. In the checkerboard resolution test, positive and negative velocity perturbations of 2% are assigned to the 3D grid nodes that are arranged in the modeling space. The resolution is considered to be good for the areas where the checkerboard image is reconstructed. In the restoring test, the 3D model obtained from the real inversion (Fig. 12a–c) is taken as the input velocity model.

The resolution is good for the entire Hainan island in the shallow crust (Fig. 13a–c) and the uppermost mantle (Fig. 13f), while in the middle and lower crust it is relatively poor (Fig. 13d and e). This is due to the fact that most local earthquakes in this region occurred in the upper and middle crust (Fig. 11a–d). At 70–120 km depth the resolution is good in the entire Hainan island (Fig. 13g and h), but at 170 km depth and deeper portions the good-resolution area biases toward the east (Fig. 13i–l), because many rays come from the teleseismic events in the western Pacific subduction zones

(Figs. 3b and 5). In order to see more clearly the main features in our images, we displayed the results of the checkerboard test along the corresponding vertical cross sections (Fig. 14) using the star-cross way through which it is easy and straightforward to understand where the resolution is good and where it is poor (e.g., Lei and Zhou, 2002; Lei and Zhao, 2005, 2007a,b). Stars denote the grid nodes where the pattern of the input velocity anomalies is retrieved correctly after the inversion, while crosses denote the grid nodes where the pattern of the input velocity anomalies is wrongly recovered after the inversion. The size of star and cross symbols denotes the ratio of the inverted amplitude of the velocity anomaly to that in the input model. It is found that the resolution is good along these three cross sections (Fig. 14), though the amplitude of anomalies at some grid nodes is not completely retrieved (Fig. 14a and b).

To further confirm the main features of our obtained image, a number of synthetic tests have been carried out by assuming different geometries of low-V anomalies in the input models. Among them, five synthetic tests are illustrated in Fig. 15. The first three
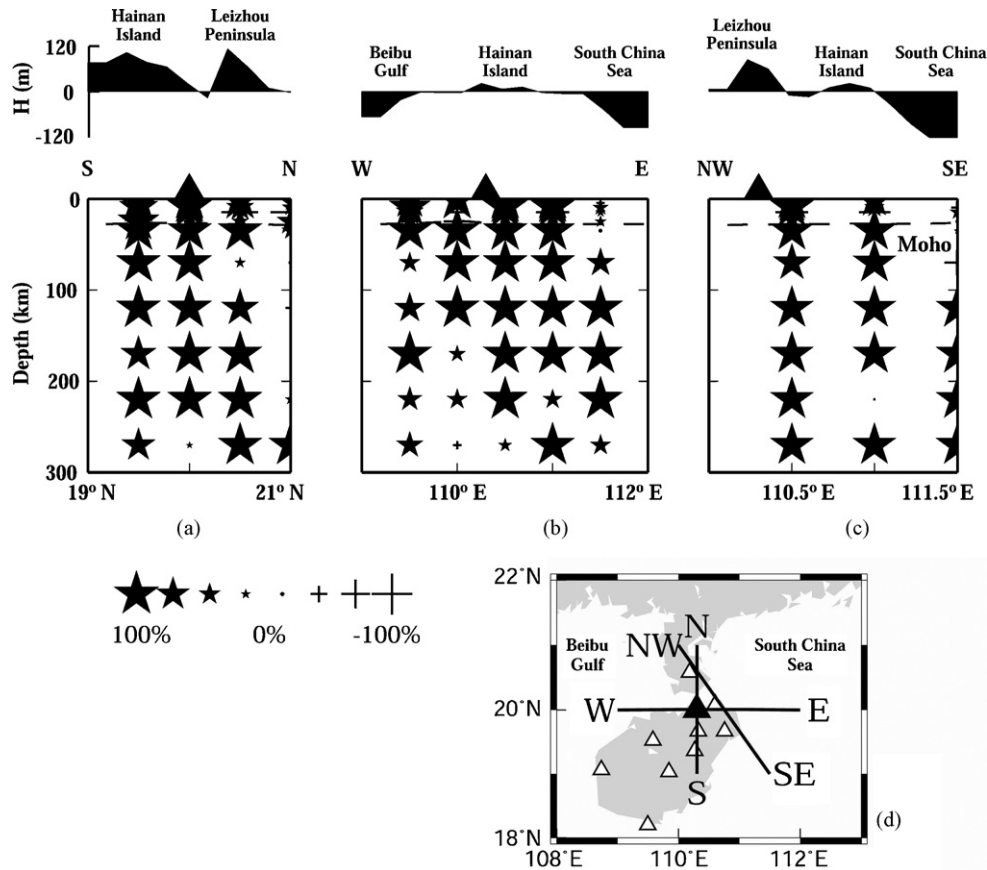
Fig. 14. The same as Fig. 13 but for the vertical cross-sections. Star-cross way is used to express the resolution (Lei and Zhou, 2002; Lei and Zhao, 2005, 2007a). Stars denote the grid nodes where the pattern of the input velocity anomalies is retrieved correctly after the inversion, that is, fast velocity anomalies in the input model are recovered to be fast, and slow ones in the input model are recovered to be slow after the inversion, while crosses denote the grid nodes where the pattern of the input velocity anomalies is wrongly recovered after the inversion. The size of star and cross symbols denotes the ratio of the inverted amplitude of the velocity anomaly to that in the input model. The stars with values of 100% show the grid nodes where the checkerboard pattern is recovered perfectly. The scale for the degree of recovery (in %) is shown at the bottom. Locations of cross-sections are shown at the bottom.

tests have low-V anomalies of up to −2% in the input model right under the Hainan hotspot from the surface to depths of 150, 250 and 300 km, respectively (Fig. 15a, b, e, f, i and j). The low-V anomaly in the input model of the fourth test is similar to that in the third test, but there is no velocity anomaly between 150 and 250 km depths (Fig. 15m and n). The fifth test is to input low-V anomalies beneath the Hainan hotspot (Fig. 15q) that are quite similar to those in our final image (Fig. 12c). Note that in the input model the shape of the velocity anomaly is assumed to be cylindrical. The purpose of the first three tests is to confirm whether low-V anomalies right beneath the Hainan hotspot only extend down to 150 km depth (Fig. 15a–l). The objective of the third and fourth tests is to make sure whether low-V anomalies right beneath the Hainan hotspot around 250–300 km depth are reliable (Fig. 15i–p). The aim of the fifth test is to affirm whether the geometry of the southeastward deflected plume with depth is a real feature (Fig. 15q and r). Fig. 15a–d shows that the resolution of the image above 150 km depth is better than that at depths of 150–250 km (Fig. 15e–h), but the data used cannot differentiate a continuous structure below 250 km depth (Fig. 15i–p). Fig. 15q–r suggests that our data cannot resolve well the structure below 250 km depth but can resolve the structure above 250 km depth, in particular near 110.5° E. These synthetic tests suggest that the low-V anomaly right beneath the Hainan hotspot around 250–300 km depth is not reliable (Fig. 12a–c), being consistent with the results of the checkerboard resolution test (Figs. 13k,l and 14a,b) and a relatively poor coverage of rays around these depths (Fig. 5c), but the south-

eastward deflection of the low-V anomaly under the Hainan hotspot is a robust feature (Fig. 12c).

From the results of the restoring test (Fig. 16), it can be seen that, although the amplitude of velocity anomalies is not fully recovered along the three vertical cross-sections, the pattern of anomalies is the same as that derived from real data (Fig. 12a–c). Note that the low-V anomaly right beneath the Hainan hotspot around 300 km depth is almost not recovered (Fig. 16a and b), indicating that this low-V feature is not robust. This is similar to the results from the checkerboard resolution test (Figs. 13k,l and 14a,b) and the synthetic tests (Fig. 15i–p). In conclusion, these extensive resolution tests all demonstrate that the main feature, a southeastward deflected plume, revealed by our present study is reliable.

5. Discussion

5.1. Effect of the local and teleseismic data

To investigate how the local and teleseismic data used contribute to our resulting crustal images, we conducted two more tomographic inversions by separately using the local and teleseismic data in the same parameterized model in the crust to the upper mantle (Figs. 12d–f and 17d–i). It is found that when only the local data are used, the pattern and velocity amplitude of the crustal model correlate well with those inferred from both local and teleseismic data, but there are some significant differences between them in details (Fig. 17a–f). The model without the teleseismic

data shows discontinuous low-V anomalies in the crust under the Hainan hotspot (Fig. 17d–f). When the teleseismic data are added, the model illustrates a continuous low-V anomaly under the Hainan hotspot from the uppermost mantle to the surface (Fig. 17a–c). However, the tomographic images exhibit remarkable differences in the pattern between the model from only the teleseismic data and that from both the local and teleseismic data. The model without the local data shows a weak column-shaped high-V anomaly detected under the Hainan hotspot in the entire crust and some weak low-V anomalies observed in the lower crust to the uppermost mantle (Fig. 17g–i). Some similarities still exist between these two models, for example, some high-V anomalies under the Hainan hotspot are also observed at 5–20 km depth in the both models as

shown in Fig. 17d–i. All these results suggest that the crustal model can be determined by using only the local data. The teleseismic data also contain useful structural information on the crust, and they are generally consistent with the local data for the crust, but the teleseismic data alone cannot determine the 3D crustal image, because the local rays are nearly horizontal and the teleseimic rays are approximately vertical in the crust (Fig. 5).

To understand how the local data affect the upper mantle structure, we have compared the upper mantle models determined with and without the local data. Both models illustrate a column-shaped and southeastward deflected low-V anomaly under the Hainan hotspot in the upper mantle, quite similar in the pattern and amplitude of velocity anomalies (Fig. 12). However, some significant
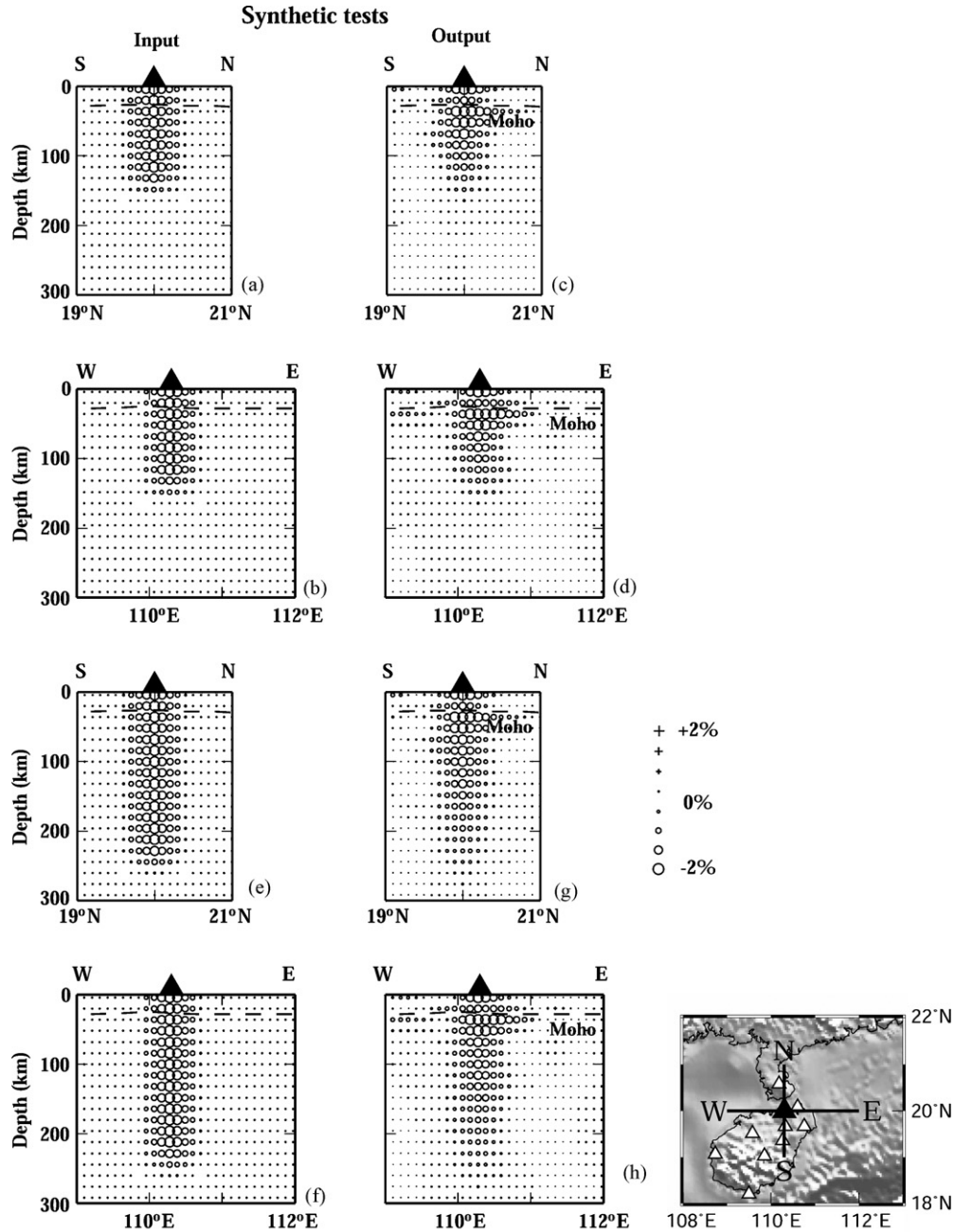
Fig. 15. Five synthetic tests. Left (a, b, e, f, i, j, m, n, q) and right (c, d, g, h, k, l, o, p, r) panels show input and output models, respectively. Open circles and crosses denote slow and fast velocity anomalies. Velocity perturbations of up to −2%, relative to the 1D velocity model as shown in Fig. 7, are assigned to the 3D nodes in the input model. The velocity perturbation scale (in %) is shown on the right sides of the panels (g, o and r). Black triangles denote the Hainan hotspot. Dashed lines denote the Moho discontinuity. Locations of cross sections are shown on the insert map. Open triangles in the insert map denote the seismic stations used.

Synthetic tests

Fig. 15. (*Continued*)
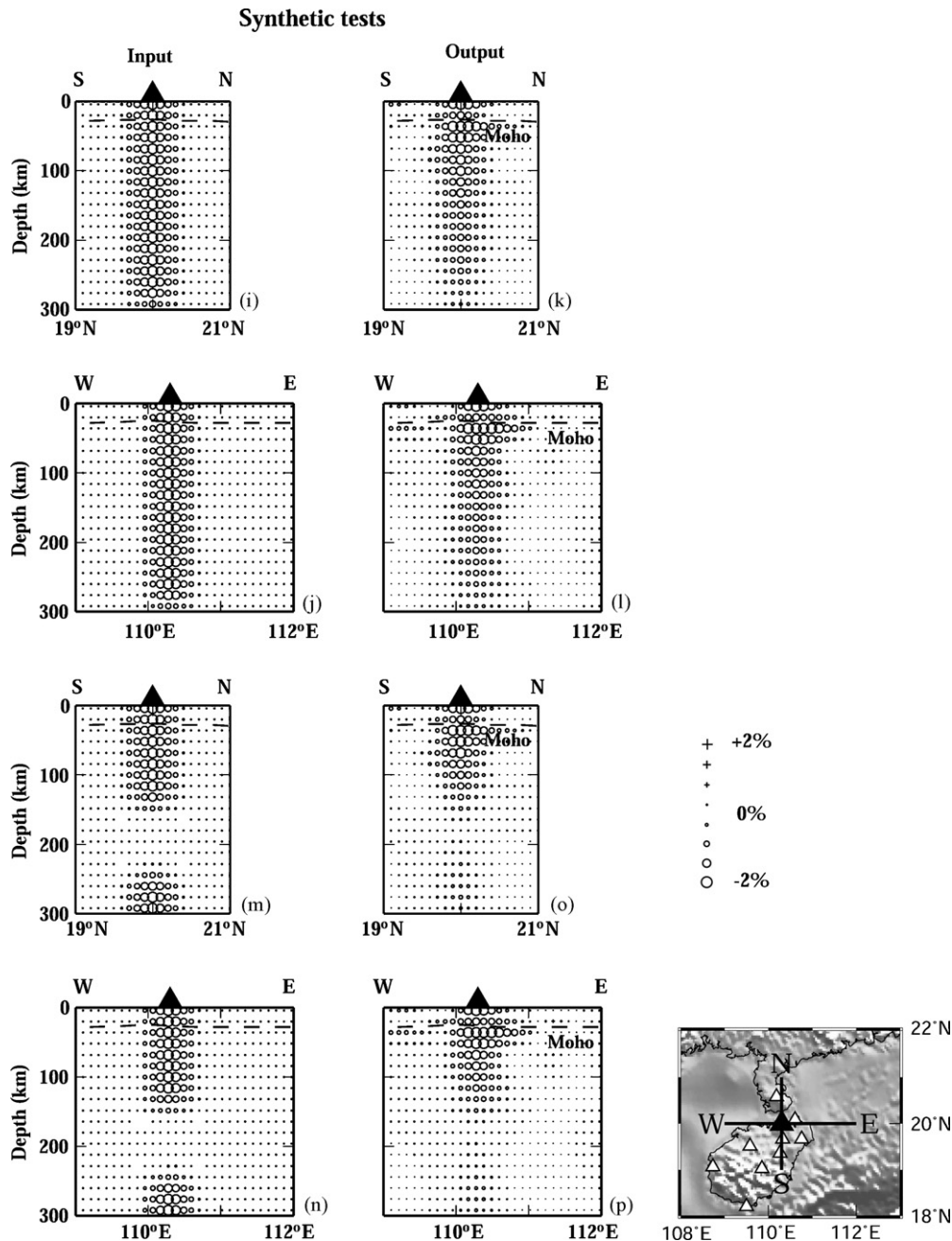
differences still exist in the morphology of anomalies between the two models. The model determined with both the local and tele-seismic data shows a clearer image of the mantle plume (Fig. 12a–c). These results suggest that it is of importance to add the local data when we determine the upper mantle structure. Therefore, in the following we discuss the surface fault zones, tectonics, and mor-phology of the plume using the 3D model obtained with both the local and teleseismic data.

5.2. Deep structure of the fault zones

In the region major active faults can be divided into two sub-groups. One is W–E oriented, while the other is NW–SE oriented. Our present results show some correlations between the faults and the velocity anomalies in the crust. The W–E oriented Wangwu-Wenjiao fault is an obvious boundary between high- and low-V anomalies. North of this fault a striking low-V anomaly is visible, which corresponds to the depression region where many volca-noes exist, while south of this fault a high-V anomaly is observed, which corresponds to the stable and uplifted region (Fig. 11a–d). This correlation extends down to the upper mantle, though exten-sive low-V anomalies are detected in the entire eastern portion of the region (Fig. 11e and f), suggesting that the Wangwu-Wenjiao fault may have cut through the Moho discontinuity to the upper mantle. Such a lithosphere-scale fault is somewhat similar to the Zhang-Bo fault in North China and the Red-River fault in Southwest China (Ma, 1987; Lei et al., 2008a,b).

In northeast Hainan, an obvious low-V anomaly is visible at 1 km depth along the NW–SE faults, i.e., Changliu-Xiangou, Haikou-Yunlong, and Puqian-Qinglan faults (Fig. 11a), while at 5 km depth
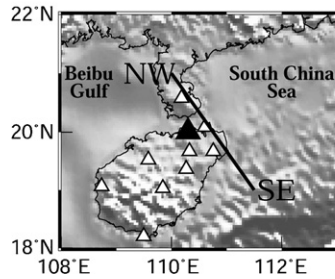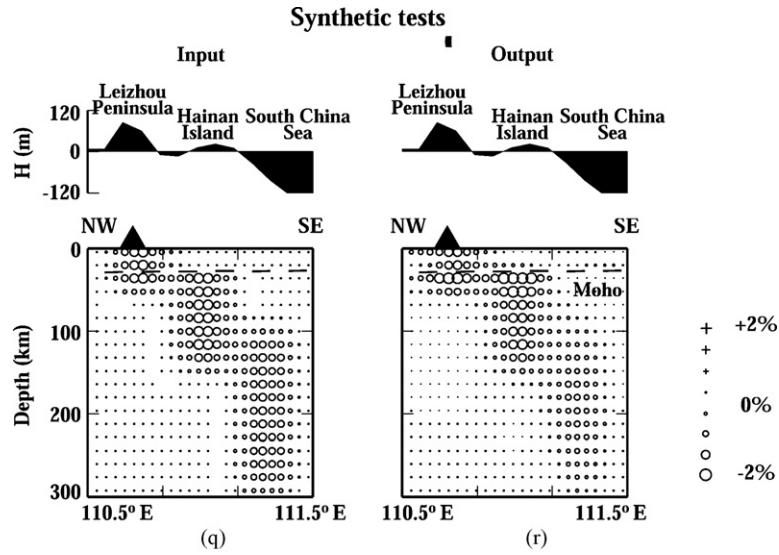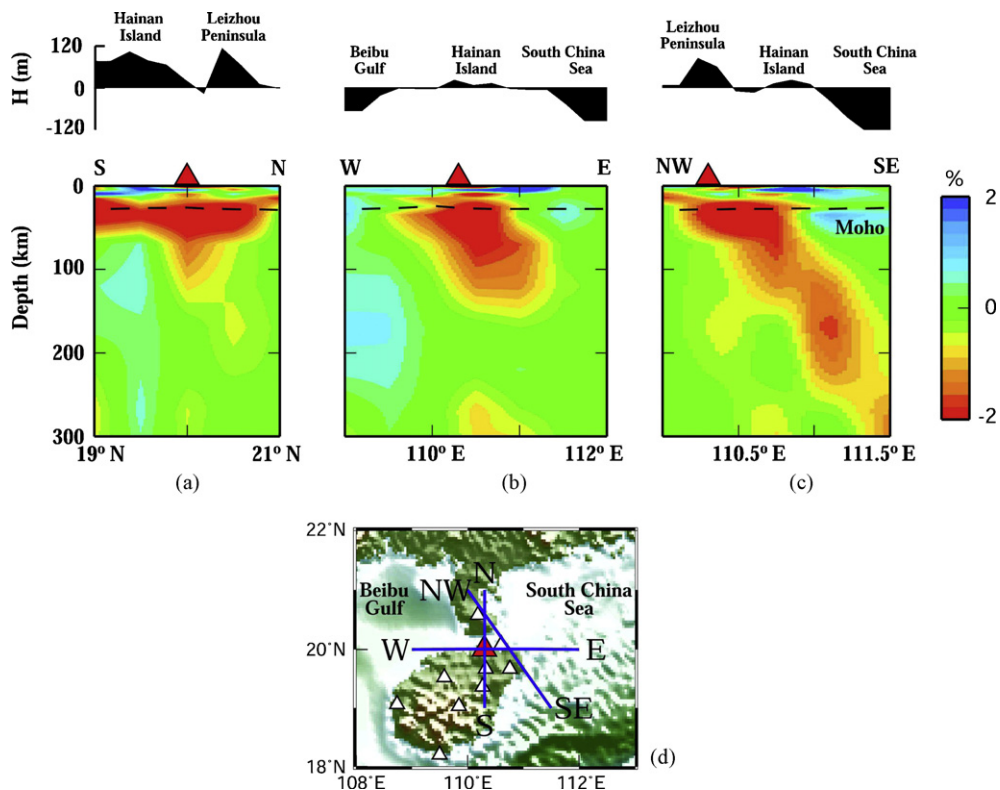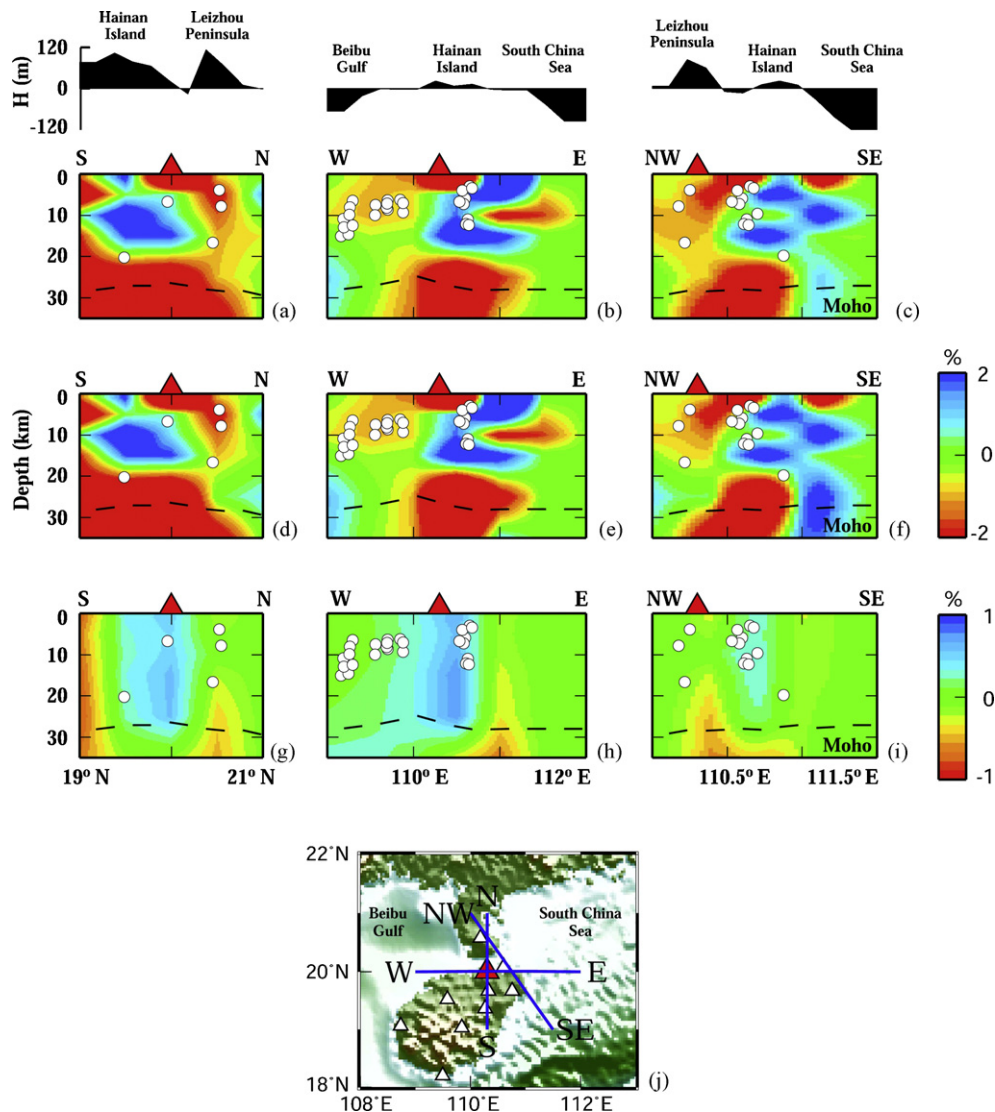
Fig. 15. (*Continued*).

Fig. 16. Output model of a restoring test using the same inversion technique and the same data set with the Gaussian noise of 0.1 s. The input model is the tomographic model as shown in Fig. 12a–c.

Fig. 17. (a–c) The same as parts (a–c) of Fig. 12 but for the depth range of 0–35 km. (d–f) The crustal images determined by using only the local data. (g–i) The crustal images inferred from only the teleseismic data. The velocity perturbations of (a–f) and (g–i) are shown on the right of (f) and (i), respectively. Note that the same parameterization is used in these three models from the crust to the upper mantle. The vertical exaggeration of the tomographic images is 5:1.

these NW–SE oriented faults are located on the margin of high-V anomalies (Fig. 11b). At greater depths these faults exhibit obvious high-V anomalies (Fig. 11c and d). These results suggest that the NW–SE oriented faults may be very active but appear to be shallower. The depth extent of the faults can hardly be determined in the present study because the width of the faults should be much thinner than the resolution scale of our tomographic image. Therefore, further efforts should be made to deploy more seismic stations across these faults to better understand the seismogenic faults.

5.3. Causes of the Qiongshan earthquake

In the region a number of small earthquakes occurred on the margin of Hainan island (Fig. 2). In particular, in northeast Hainan some of them are located around the NW-SE faults and in or around high-V anomalies (Fig. 11a–f).

In addition to these small earthquakes, in the region there occurred 15 strong earthquakes (M > 5.0) since 1524 (Fig. 2). Among them, the 13 July 1605 Qiongshan earthquake (M 7.5), related to the

activity of the Puqian-Qinglan fault, was one of the most destructive earthquakes in South China. It was felt over 600 km far away from the hypocenter and killed several thousand people within Qiongshan city and 80–90% in the suburbs (Chen and Huang, 1979), and it was a unique earthquake in the history of China that caused the land with about 72 villages to sink below the sea level (Hu et al., 2007). The vertical motion was, on average, 3–4 m and amounted to 10 meters in some places. The sunken areas were as large as 100 km² (Xu, 2006). Some researchers suggested that the occurrence of the Qiongshan earthquake was closely related to the upwelling of the Hainan plume that caused the extensional stresses leading the normal fault (the Puqian-Qinglan fault) to slip (e.g., Xu, 2006; Hu et al., 2007). This is also supported by the source mechanism solutions of small earthquakes in Northeast Hainan (Diao et al., 2007), but fluids from the rising plume may have also played an important role in the generation of the Qiongshan earthquake.

The hypocenter of the Qiongshan earthquake is far from the subducting slab and is located in a volcanic area of Northeast Hainan. Our tomographic results illustrate obvious high-V anomalies above

15–20 km depth and low-V anomalies below this depth under the Qiongshan hypocenter (Figs. 11 and 17a–c), suggesting that the connection between the plume upwelling in the mantle and crustal magmatic and volcanic activity is complicated. Such a structure is in good agreement with a recent magnetotelluric image that displays a low-conductivity body above 13 km depth and a high-conductivity body extending from 13 km depth down to the upper mantle in the region (Hu et al., 2007). Moreover, previous studies also indicate that the focal depth of the Qiongshan earthquake is ~13 km (Zhang et al., 1990). These results suggest that the Qiongshan source areas are underlain by low-V and high-conductivity anomalies which are interpreted to be a fluid-filled, fractured rock matrix that contributed to the initiation of the Qiongshan earthquake. The fluids may come from the upward intrusion of the hot and wet asthenospheric materials (or partial melts) of the plume rising from the deep mantle. When the fluids enter the active Puqian-Qinglan fault, the fault zone friction may decrease and thus faulting could be triggered to generate the Qiongshan earthquake.

A similar structure was also found in the source areas of the 1976 Tangshan earthquake (M 7.8) in North China (Huang and Zhao, 2004; Lei et al., 2008a), the 1995 Kobe earthquake (M 7.2) in Japan (Zhao et al., 1996), and the 2001 Bhuj earthquake (M 7.6) in India (Mishra and Zhao, 2003), suggesting that the low-V anomalies may be associated with crustal fluids. However, the fluids under the Kobe earthquake are considered to originate from the dehydration of the subducting Philippine Sea slab (Zhao et al., 1996), while the Tangshan earthquake may be related to the deep dehydration of the Pacific slab that is stagnant in the mantle transition zone under Eastern China (Lei et al., 2008a).

Therefore, we consider that the generation of the Qiongshan earthquake may be not only associated with the extensional stresses resulting from the upwelling of the mantle plume, but also related to fluids from the rising plume.

### 5.4. Deflection of the Hainan plume

Our present results show that the middle and upper crustal velocities in northern Hainan and southern Leizhou peninsula are much lower than those in central and southern Hainan (Figs. 11 and 17a–c). This is supported by many geophysical observations such as a thinned crust (Li et al., 2006) (see Fig. 8), a relatively higher geothermal background (Chen et al., 1991) from northern Hainan to southern Leizhou peninsula, and an obvious low-resistivity anomaly (Hu et al., 2007) in northern Hainan. It is also consistent with the previous seismic results like local tomography using data from a temporary seismic network (Ding et al., 2004), deep seismic soundings (Jia et al., 2006), and Pn tomography (Liang et al., 2004). Such a pattern of seismic velocity anomalies in the crust corresponds to the uplifts in central and southern Hainan and depressions in northern Hainan. These observations suggested that the Quaternary volcanoes (Fig. 2) are quite active and erupted many times in southern Leizhou peninsula and the entire Leiqiong basin. Furthermore, the Cenozoic basalts in northern Hainan display the eruption morphology and isotopic ratios typical of hotspot volcanism (Tu et al., 1991). Lebedev et al. (2000) and Yang and Zhou (2001) suggested a thinned mantle transition zone under Hainan from their receiver-function analyses. These results all indicate the existence of the Hainan plume, or the intrusion of hot mantle materials to the crust as proposed by Sun et al. (1988).

Surface-wave tomographic studies of East Asia also display obvious low-V anomalies under Hainan down to a depth of 450 km (Friederich, 2003) or deeper to 660 km (Lebedev and Nolet, 2003). Mantle body-wave tomography of East Asia shows a broad low-V zone under Southeast Asia including Hainan down to 1300 km depth (Huang and Zhao, 2006). Global tomographic models all show a prominent and rather broad low-V anomaly under the Hainan region down to 1900 km depth (e.g., Ritsema et al., 1999; Montelli et al., 2006) or deeper to the lowermost mantle (e.g., Zhao, 2001; Antolik et al., 2003; Lei and Zhao, 2006a). These tomographic results all support the existence of the Hainan plume, but these models are still too coarse to resolve a plume-like structure under the Hainan hotspot in the upper mantle. Our present results are much improved over the previous models and provide a high-resolution velocity model down to 300 km depth, indicating that the plume has a diameter of about 80 km (Fig. 12c), which is much thinner than the diameter (about 400 km) estimated by the previous studies (e.g., Montelli et al., 2006). Because viscosity in the plume is expected to be lower in the upper mantle than in the lower mantle, the plume is expected to be thinner in the upper mantle. Furthermore, our image shows that the Hainan plume conduit is inclined toward the southeast from the surface (Fig. 12a–c). A number of resolution tests all demonstrated that these main features obtained are reliable (Figs. 13–16).

Deflection of the plume is also found under Hawaii, Iceland and Africa (e.g., Ritsema et al., 1999; Zhao, 2001; Bijwaard and Spakman, 1999; Lei and Zhao, 2006b; Nolet et al., 2007), possibly owing to mantle flow (e.g., Zhao, 2001; Nolet et al., 2007). However, these global models usually exhibit remarkable inclination of the plume in the middle and lower mantle rather than in the upper mantle, possibly due to their limited spatial resolution of the upper mantle. Recently, Yang et al. (2006) imaged the Azores plume in the shallow mantle, and found a northeastward tilting low-V anomaly under the Azores hotspot, which was explained in part due to the upper mantle flow driven by the absolute plate motion of the African and Eurasian plates. Hainan island is located in an area of convergence between the Eurasian plate, Indian plate and Philippine sea plate, hence the deflection of the plume conduit may be associated with the subduction of oceanic plates, especially the Philippine sea plate, and the extrusion of the Eurasian plate toward the southeast, away from the Tibetan plateau. This extrusion by itself is expected to cause a plume conduit tilt in the opposite sense of what is observed. Most likely, the tilted plume conduit has buoyantly risen from the lower mantle, as discussed below.

The imaged shape of what is interpreted to be the Hainan plume conduit can be compared with the shape of the plume conduit predicted from a geodynamic model of plumes in large-scale mantle flow. The model (Steinberger and Antretter, 2006) essentially assumes that the motion of each part of the conduit can be computed as a superposition of advection in large-scale mantle flow and buoyant rising. A tilted plume conduit may thus result from shear flow. However, due to buoyant rising, shearing in a deeper part of the mantle may also cause a tilted conduit less deep in the mantle at a later time. In particular, strongly tilted conduits may occur in regions of large-scale downward flow, as parts of the conduit may get dragged down with the flow. This may also have happened to the Hainan plume, because lithospheric slabs have been inserted and presumably sunk into the mantle at a number of subduction zones in the region (e.g., Zhao, 2001; Lei and Zhao, 2006a). Geochemical composition also reflects a slab-derived component in the mantle source (Zhu and Wang, 1989; Tu et al., 1991; Flower et al., 1992; Zhang et al., 1996). Large-scale mantle flow is computed based on global tomography interpreted as density anomalies that drive flow. It is time dependent, because plate motions that are used as surface boundary condition change with time, and the advection of density heterogeneities in large-scale flow is considered. Beneath the Hainan region, computed flow in the lowermost mantle is towards the southeast, towards a large upwelling beneath the south-central Pacific (sometimes referred to as the Pacific superplume), away from what has been interpreted as Mesozoic subducted slabs under Siberia (van der Voo et al., 1999), and it is stronger at 50 Ma (as
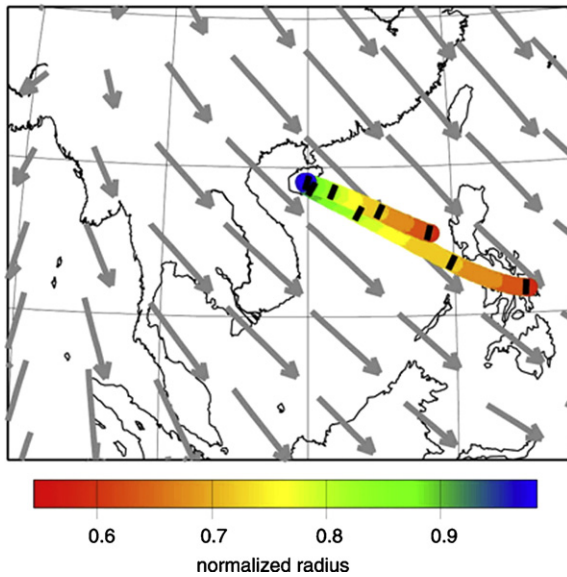
Fig. 18. Computed Hainan plume conduit shapes. The plume source is moving with large-scale flow; plume buoyancy flux is 10^3 kg/s. The two conduits are for different assumed ages of origin, 100 and 50 Ma. Color indicates depth; scale is shown at the bottom. Other modeling assumptions are the same as that in Fig. 13 of Steinberger and Antretter (2006). Gray arrows denote the horizontal flow component in the lowermost mantle (at 2512 km depth) at 50 Ma. Arrow length scale is 5° of arc per cm/year. Grid spacing is 10°.

shown in Fig. 18) than it is now. In contrast, the computed horizontal flow component in the upper part of the lower mantle and the transition zone beneath the region is approximately towards the west, with smaller speed. Thus, shearing between southeastward flow in the lowermost mantle and slower westward flow around ∼660 km depth causes a tilted plume conduit in the lower mantle. Two results are shown in Fig. 18. The assumed anomalous mass flux 10^3 kg/s is a generic value typical for medium-size plumes, and generally predicted plume conduit shapes do not strongly change even if this value is changed by a factor of 2 or 3 (Steinberger and Antretter, 2006). Computed tilt is stronger for older plume initiation age (at which time a vertical plume conduit is assumed) 100 Ma than for age 50 Ma, both because the conduit has been sheared for a longer time, and computed flow in the lowermost mantle is stronger for earlier times. On the other hand, the predicted conduit shape is close to vertical in the upper mantle. At face value, this is in contrast with seismic images that show a plume conduit that is tilted in the upper mantle. However, since a tilted conduit may have buoyantly risen from the lower mantle, the observed tilt in the upper mantle may correspond to the predicted tilt in the lower mantle, with approximately the same direction and amount. Other causes for a conduit predicted to be tilted in the upper mantle are shearing due to fast plate motions (e.g., for Hawaii) or due to a strong large-scale horizontal asthenospheric flow component (e.g., for Yellowstone). However, plate motion in the Hainan region is slow compared to the Pacific plate motion in the vicinity of Hawaii, and flow models rather predict asthenospheric flow approximately radially away from Hainan towards the surrounding subduction zones. Hence, the explanation that the tilted conduit has buoyantly risen from the lower mantle appears most likely, and supports the lower mantle origin of the Hainan plume, as is also inferred from some other tomographic images (e.g., Zhao, 2001; Antolik et al., 2003; Lei and Zhao, 2006a) as discussed above. An implication of this explanation is that the hotspot (surface expression of the tilted conduit) moves southeastward as the tilted conduit rises to the surface, and thus could cause an age-progressive "hotspot track" with volcanism

getting progressively younger towards the southeast. In contrast, motion of South China lithosphere over a stationary hotspot would cause a hotspot track with ages getting older towards the east to southeast. In practice, such an age progression may be difficult to establish, in particular in continental lithosphere, because volcanism may continue for a substantial time period after the hotspot has passed. Nevertheless, the present location of the hotspot beneath northeastern Hainan in combination with late Tertiary and Quaternary volcanism also occurring on Leizhou peninsula, towards the northwest of the present-day hotspot location, supports the trend predicted due to rise of a titled conduit. The expected age progression depends on the amount of tilt and buoyant plume rising speed. The latter can also be estimated from the model of Steinberger and Antretter (2006). For an anomalous mass flux 10^3 kg/s the predicted centerline temperature anomaly is about 150 K in the upper mantle, corresponding to about 2% seismic velocity anomaly, which agrees well with the observed anomaly (Figs. 11 and 12a–c). From this temperature anomaly, the viscosity inside the conduit, and a plume conduit diameter of about 160 km in the upper mantle can be inferred. Steinberger and Antretter (2006) infer from a plume diameter of ∼160 km a buoyant rise time of ∼4 Ma from a depth of 250 km to the surface which, with the observed tilt, implies an age progression of about 25 km per Ma. However, the tomographic model (Fig. 12a–c) shows the Hainan plume only about half as wide, in which case buoyant rise speed would be reduced by about a factor of 4, and a reduced age progression of about 6 km per Ma would be expected.

Therefore, further efforts should be made to deploy many portable seismic stations in and around Hainan island and combine body-wave with surface-wave observations (West et al., 2004) and/or employ the finite-frequency tomographic method (e.g., Hung et al., 2004; Montelli et al., 2004a; Tromp et al., 2005) to better image the Hainan plume in both the upper and lower mantle.

6. Conclusions

A high-resolution tomographic model of the upper mantle has been determined beneath Hainan island and adjacent areas, and the configuration of the Hainan plume in the upper mantle has, for the first time, been revealed by using high-quality local and teleseismic data. The Hainan plume is imaged as a continuous low-V column extending from the surface down to 250 km depth with a diameter of about 80 km. This low-V anomaly is tilted towards the southeast, being consistent with the plume conduit predicted by numerical modeling. Such an inclination may be associated with the subduction of oceanic plates, in particular the Philippine sea plate, and the extrusion of the Eurasian plate, but most likely the tilted plume conduit has buoyantly risen from the lower mantle. Distortion of the conduit in the lower mantle may be caused by large-scale mantle flow. Our present results show a much better image of the Hainan plume than those in the previous models and provide new constraints on the mantle dynamics under Southeast Asia.

References

Allen, R., Nolet, G., Morgan, W., Vogfjord, K., Bergsson, B., Erlendsson, P., Foulger, G., Jakobsdottir, S., Julian, B., Pritchard, M., Ragnarsson, S., Stefansson, R., 2002. Imaging the mantle beneath Iceland using integrated seismological techniques. J. Geophys. Res. 107, doi:10.1029/2001JB000595.

Antolik, M., Gu, Y., Ekstrom, G., Dziewonski, A., 2003. J362D28: a new joint model of compressional and shear velocity in the Earth's mantle. Geophys. J. Int. 153, 443–466.

Barmin, M., Ritzwoller, M., Levshin, A., 2001. A fast and reliable method for surface wave tomography. Pure Appl. Geophys. 158, 1351–1375.

Bijwaard, H., Spakman, W., 1999. Tomographic evidence for a narrow whole mantle plume below Iceland. Earth Planet. Sci. Lett. 166, 121–126.

Boschi, L., 2003. Measures of resolution in global body wave tomography. Geophys. Res. Lett. 30, doi:10.1029/2003GL018222.

Boschi, L., 2006. Global multiresolution models of surface wave propagation: comparing equivalently regularized Born and ray theoretical solutions. Geophys. J. Int. 167, 238–252.

Boschi, L., Becker, T., Soldati, G., Dziewonski, A.M., 2006. On the relevance of Born theory in global seismic tomography. Geophys. Res. Lett. 33, doi:10.1029/2005GL025063.

Chen, Y., Huang, Y., 1979. Preliminary discussion on the 1605 Qiongzhou earthquake and its seismogenetic structure. Seismol. Geol. 1 (4), 37–44.

Chen, M., Xia, S., Yang, S., 1991. Local geothermal anomalies around Leizhou peninsula and its mechanism. Geol. Sci. 4, 369–383.

Chen, Y., Xi, D., Fan, X., 2002. Analyses of active faults using the theory of subseparation. Earthquake Res. 25 (4), 351–355.

Courtillot, V., Davaille, A., Besse, J., Stock, J., 2003. Three distinct types of hotspots in the Earth's mantle. Earth Planet. Sci. Lett. 205, 295–308.

Davies, G., 1988. Ocean bathymetry and mantle convection 1. Large-scale flow and hotspot. J. Geophys. Res. 93, 10467–10480.

Diao, G., Zhang, X., Zhang, X., Sun, Q., Wang, X., 2007. The source mechanism solution to small earthquakes in northeast Hainan (in manuscript).

Ding, Z., Li, W., Wu, Q., Hu, J., He, Z., Zhang, L., 2004. Seismological observations and velocity structure of the crust and upper mantle in the north Hainan volcanic region. In: Zhang, Z., Gao, R., Lv, Q., Liu, Z. (Eds.), Earth's Deep Structure and Dynamics of Mainland China—the 50th Anniversary of Academician Teng Working for Geophysics. Scientific Press, Beijing, pp. 846–857.

Dziewonski, A., Gilbert, F., 1976. The effect of small aspherical perturbations on travel times and a re-examination of the corrections for ellipticity. Geophys. J. R. Astron. Soc. 44, 7–17.

Eberhart-Phillips, D., 1986. Three-dimensional velocity structure in Northern California Coast Ranges from inversion of local earthquake arrival times. Bull. Seismol. Soc. Am. 76, 1025–1052.

Ekström, G., Tromp, J., Larson, E., 1997. Measurements and global models of surface wave propagation. J. Geophys. Res. 102, 8137–8157.

Engdahl, R., van der Hilst, R., Buland, R., 1998. Global teleseismic earthquake relocation with improved travel times and procedures for depth determination. Bull. Seism. Soc. Am. 88, 722–743.

Flower, M., Zhang, M., Chen, C., Tu, K., Xie, G., 1992. Magmatism in the South China Basin, 2. Post-spreading Quaternary basalts from Hainan Island. South China Chem. Geol. 97, 65–87.

Friederich, W., 2003. The S-velocity structure of the East Asian mantle from inversion of shear and surface waveforms. Geophys. J. Int. 153, 88–102.

Hansen, P., 1992. Analysis of discrete ill-posed problems by means of the L-curve. SIAM Rev. 34, 561–580.

Ho, K., Chen, J., Juang, W., 2000. Geochronology and geochemistry of late Cenozoic basalts from the Leiqiong area, southern China. J. Asian Earth Sci. 18, 307–324.

Hu, J., Deng, B., Wang, W., Lin, Z., Xiang, X., Wang, L., 2007. Deep electronic anomaly in the M7.5 Qiongshan earthquake region and its relationship with future seismicity. Acta Seismol. Sinica 29 (3), 258–264.

Hu, J., Chen, J., Huang, M., 1997. Analyses on the characteristics of 1995 (M 5.2) Dongfang earthquake, Hainan. South China J. Seismol. 17 (1), 39–45.

Huang, J., Zhao, D., 2004. Crustal heterogeneity and seismotectonics of the region around Beijing, China. Tectonophysics 385, 159–180.

Huang, J., Zhao, D., 2006. High-resolution mantle tomography of China and surrounding regions. J. Geophys. Res. 111, doi:10.1029/2005JB004066.

Hung, S., Shen, Y., Chiao, L., 2004. Imaging seismic velocity structure beneath the Iceland hot spot: a finite frequency approach. J. Geophys. Res. 109, doi:10.1029/2003JB002889.

Jia, S., Li, Z., Xu, C., Shen, F., Zhao, W., Yang, Z., Yang, J., Lei, Y., 2006. Crust structure features in Leiqiong depression. Chinese J. Geophys. 49 (5), 1385–1394.

Kennett, B., Engdahl, E., 1991. Traveltimes for global earthquake location and phase identification. Geophys. J. Int. 105, 429–465.

Lebedev, S., Chevrot, S., Nolet, G., van der Hilst, R., 2000. New seismic evidence for a deep mantle origin of the S. China basalts (the Hainan plume?) and other observations in SE Asia. EOS Trans. AGU 81, 48–148.

Lebedev, S., Nolet, G., 2003. Upper mantle beneath Southeast Asia from S velocity tomography. J. Geophys. Res. 108, doi:10.1029/2000JB000073.

Lei, J., Xie, F., Lan, C., Xing, C., Ma, S., 2008a. Seismic images under the Beijing region using P and PmP data. Phys. Earth Planet. Inter. 168, 134–146.

Lei, J., Zhao, D., Su, Y., 2008b. Insight into the origin of the Tengchong intraplate volcano in southwest China from local and teleseismic data. J. Geophys. Res. revised.

Lei, J., Zhao, D., 2005. P-wave tomography and origin of the Changbai intraplate volcano in Northeast Asia. Tectonophysics 397, 281–295.

Lei, J., Zhao, D., 2006a. Global P-wave tomography: on the effect of various mantle and core phases. Phys. Earth Planet. Inter. 154, 44–69.

Lei, J., Zhao, D., 2006b. A new insight into the Hawaiian plume. Earth Planet. Sci. Lett. 241, 438–453.

Lei, J., Zhao, D., 2007a. Teleseismic P-wave tomography and the upper mantle structure of the central Tien Shan orogenic belt. Phys. Earth Planet. Inter. 162, 165–185.

Lei, J., Zhao, D., 2007b. Teleseismic evidence for a break-off subducting slab under Eastern Turkey. Earth Planet. Sci. Lett. 257, 14–28.

Lei, J., Zhou, H., 2002. 3-D velocity structure of P-wave in the upper mantle beneath Southwestern China and its adjacent areas. Acta Seismol. Sinica 24 (2), 126–134.

Leveque, J., Rivera, L., Wittlinger, G., 1993. On the use of the checker-board test to assess the resolution of tomogarpic inversions. Geophys. J. Int. 115, 313–318.

Li, J., 1991. Tectonic system of faults and regional stability in Hainan island. Ocean Sci. 3, 19–21.

Li, Z., Zhao, W., Liu, G., 2006. Deep crustal structure and stress state of the 1605 Qiongzhou large earthquake. South China J. Seismol. 26 (1), 28–36.

Liang, C., Song, X., Huang, J., 2004. Tomographic inversion of Pn travel times in China. J. Geophys. Res. 109, doi:10.1029/2003JB002789.

Liu, J., 1999. Chinese volcanoes. Scientific Press, Beijing, pp. 5–8.

Liu, R., 2000. Active Volcanoes in China. Seismological Press, Beijing, pp. 75–80.

Liu, R., Zhang, Z., 1989. Characteristics of neotectonic movement in Hainan island. Trop. Geog. 9 (2), 174–182.

Ma, X., 1987. Outline of the Dynamics of Chinese Lithosphere. Geological Press, Beijing.

Ma, X., 1989. Lithospheric Dynamics Atlas of China. Cartographic Press, pp. 46–146.

Mishra, O.P., Zhao, D., 2003. Crack density, saturation rate and porosity at the 2001 Bhuj, India, earthquake hypocenter: a fluid-driven earthquake? Earth Planet. Sci. Lett. 212, 393–405.

Molnar, P., Tapponnier, P., 1975. Cenozoic tectonics of Asia: Effects of a continental collision. Science 198, 419–1421.

Montelli, R., Nolet, G., Dahlen, F., Masters, G., Engdahl, E., Hung, S., 2004a. Finite-frequency tomography reveals a variety of plumes in the mantle. Science 303, 338–343.

Montelli, R., Nolet, G., Masters, G., Dahlen, F., Hung, S., 2004b. Global P and PP travel time tomography: rays versus waves. Geophys. J. Int. 158, 637–654.

Montelli, R., Nolet, G., Dahlen, F., Masters, G., 2006. A catalogue of deep mantle plumes: new results from finite frequency tomography. Geochem. Geophys. Geosys. 7, doi:10.1029/2006GC001248.

Morgan, W., 1971. Convection plumes in the lower mantle. Nature 230, 42–43.

Nolet, G., Allen, R., Zhao, D., 2007. Mantle plume tomography. Chem. Geol. 241, 248–263.

Paige, C., Saunders, M., 1982. LSQR: an algorithm for sparse linear equations and sparse least squares. Assoc. Comput. Math. Trans. Math. Software 8, 43–71.

Qiu, X., Zeng, G., Xu, Y., Hao, T., Li, Z., Priestly, K., McKenzie, D., 2006. The crustal structure beneath the Shidao station on Xisha islands of South China Sea. Chinese J. Geophys. 49 (6), 1720–1729.

Ritsema, J., van Heijst, H., Woodhouse, J., 1999. Complex shear wave velocity structure imaged beneath Africa and Iceland. Science 286, 1925–1928.

Sleep, N., 1990. Hotspots and mantle plumes: some phenomenology. J. Geophys. Res. 95, 6715–6736.

Steinberger, B., Antretter, M., 2006. Conduit diameter and buoyant rising speed of mantle plumes: implications for the motion of hot spots and shape of plume conduits. Geochem. Geophys. Geosys. 7, doi:10.1029/2006GC001409.

Sun, J., Fan, Q., Chen, W., 1988. Quaternary volcanic activity in north Hainan. In: Ding, Y., et al. (Eds.), Collection of Papers of Earthquake Research in North Hainan. Seismological press, Beijing, pp. 17–25.

Tapponnier, P., Peltzer, G., Armijo, R., 1986. On the mechanics of the collision between India and Asia. In: Coward, M., Ries, A. (Eds.), Collision Tectonics, 19. Geological Society London Special Publication, pp. 115–157.

Tromp, J., Tape, C., Liu, Q., 2005. Seismic tomography, adjoint methods, time reversal and banana-doughnut kernels. Geophys. J. Int. 160, 195–216.

Tu, K., Flower, M., Carlson, R., Zhang, M., Xie, G., 1991. Sr, Nd, and Pb isotopic compositions of Hainan basalts (south China): implications for a subcontinental lithosphere Dupal source. Geology 19, 567–569.

van der Voo, R., Spakman, W., Bijwaard, H., 1999. Mesozoic subducted slabs under Siberia. Nature 397, 246–249.

Waldhauser, F., Ellsworth, W., 2000. A double-difference earthquake relocation algorithm: method and application to the Northern Hayward fault, California. Bull. Seism. Soc. Am. 90 (6), 1353–1368.

Wessel, P., Smith, W., 1995. New version of the Generic Mapping Tools (GMT) version 3.0 released. EOS Trans. AGU 76, 329–1329.

West, M., Gao, W., Grand, S., 2004. A simple approach to the joint inversion of seismic body and surface waves applied to the southwest US. Geophys. Res. Lett. 31, doi:10.1029/2004GL020373.

Wilson, J., 1963. A possible origin of the Hawaiian islands. Can. J. Phys. 41, 863–870.

Xu, Q., 2006. The Coseismic coast fast sinkage and the following possible Tsunami caused by the 1605 Qiongshan strong earthquake and the evidence. South China J. Seismol. 26 (1), 17–27.

Yang, T., Shen, Y., van der Lee, S., Solomon, S., Hung, S., 2006. Upper mantle structure beneath the Azores hotspot from finite-frequency seismic tomography. Earth Planet. Sci. Lett. 250, 11–26.

Yang, Y., Zhou, H., 2001. Application of receiver function method to estimate the buried depths of discontinuities in the upper mantle beneath China and adjacent area. Chinese J. Geophys. 44 (6), 783–792.

Yin, A., Harrison, T., 2000. Geological evolution of the Himalayan-Tibetan orogen. Annu. Rev. Earth Planet. Sci. 28, 211–280.

Zhang, M., Tu, K., Xie, G., Flower, M., 1996. Subduction-modified subcontinental mantle: trace element and isotope evidence in basalts from Hainan Island. Chinese J. Geochem. 15, 1–19.

Zhang, H., Chen, W., Huang, K., et al., 1990. Movement of Neotectonics and Geological Environment Along the Sea in South China. Seismological Press, Beijing, pp. 1–316.

Zhao, D., 2001. Seismic structure and origin of hotspots and mantle plumes. Earth Planet. Sci. Lett. 192, 251–265.

Zhao, D., 2004. Global tomographic images of mantle plumes and subducting slabs: insight into deep Earth dynamics. Phys. Earth Planet. Inter. 146, 3–34.

Zhao, D., Hasegawa, A., Horiuch, S., 1992. Tomographic imaging of P and S wave velocity structure beneath northeastern Japan. J. Geophys. Res. 97, 19909–19928.

Zhao, D., Hasegawa, A., Kanamori, H., 1994. Deep structure of Japan subduction zones as derived from local, regional, and teleseismic events. J. Geophys. Res. 99, 22313–22329.

Zhao, D., Kanamori, H., Negishi, H., Wiens, D., 1996. Tomography of the source area of the 1995 Kobe earthquake: evidence for fluids at the hypocenter? Science 274, 1891–1894.

Zhao, D., Lei, J., 2004. Seismic ray path variations in a 3D global velocity model. Phys. Earth Planet. Inter. 141, 153–166.

Zhao, D., Lei, J., Inoue, T., Yamada, A., Gao, S., 2006. Deep structure and origin of the Baikal rift zone. Earth Planet. Sci. Lett. 243, 681–691.

Zhou, X., Armstrong, R., 1982. Cenozoic volcanic rocks of eastern China: secular and geographic trends in chemistry and strontium isotopic composition. Earth Planet. Sci. Lett. 58, 301–329.

Zhu, B., Wang, H., 1989. Nd-Sr-Pb isotopic and chemical evidence for the volcanism with MORB-OIB source characteristics in the Leiqiong area. China Geochim. 3, 193–201.